

Effect of Sn Doping on Structural and Optical Properties of $\text{CsPb}_{1-x}\text{Sn}_x\text{Cl}_3$

A dissertation for

Course code: PHY 651

Credits: 16

Submitted in partial fulfilment of Masters Degree

M.Sc. in Physics

by

AMEY AUDOOTH BANDODKAR

Roll Number: 22P0430002

ABC ID: 322-072-577-604

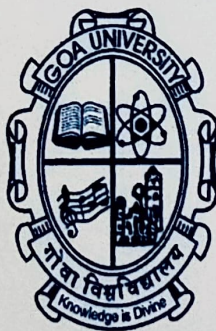
PRN: 201905803

Under the supervision of

Dr. Pranav P. Naik

School of Physical and Applied Science

Physics Discipline



Goa University

May 2024



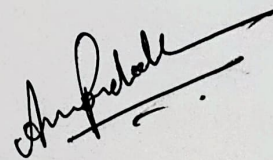
Examined by:

Seal of the School

DECLARATION BY STUDENT

I hereby declare that the data presented in this Dissertation report entitled, "Study the Effect of Sn Doping on Structural and Optical Properties of $\text{CsPb}_{1-x}\text{Sn}_x\text{Cl}_3$ " is based on the results of investigations carried out by me in the Physics Discipline at the School of Physical and Applied Sciences, Goa University under the Supervision of Dr. Pranav P. Naik. and the same has not been submitted elsewhere for the award of a degree or diploma by me. Further, I understand that Goa University or its authorities will be not be responsible for the correctness of observations / experimental or other findings given the dissertation.

I hereby authorize the University authorities to upload this dissertation on the dissertation repository or anywhere else as the UGC regulations demand and make it available to any one as needed.



Name: Mr. Amey A. Bandodkar

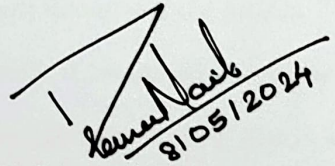
Roll no:22PO430002

Date: 08/05/2024

Place: Goa University

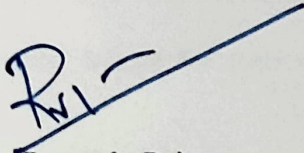
COMPLETION CERTIFICATE

This is to certify that the dissertation report “Study the Effect of Sn Doping on Structural and Optical Properties of $\text{CsPb}_{1-x}\text{Sn}_x\text{Cl}_3$ ” is a bonafide work carried out by Mr. Amey A. Bandodkar under my supervision in partial fulfilment of the requirements for the award of the degree of M.Sc. in Physics at the School of Physical and Applied Sciences, Goa University.


8/05/2024

Signature and name of Supervising Teacher: Dr. Pranav P. Naik

Date: 8/05/2024



Dean: Prof. Dr. Ramesh. Pai.

Date: 8/05/2024

Place: Goa University



School Stamp

ACKNOWLEDGEMENT

I am pleased to present the report of my project work undertaken during my final year in M.Sc. Physics. Although I have worked hard for the success of this project, it would not have been possible without the help and guidance of some people. Therefore, I would like to express my deep gratitude to those individuals.

Firstly, I would like to thank my project guide, Dr. Pranav P. Naik, for his excellent guidance, encouragement, intelligence and invaluable insight throughout the project. Thank you, Sir, for always motivating and inspiring me. Secondly, I would like to thank Ms. Sugania Chandavelou for her constant help and support throughout the project. Also, I would like to express my heartfelt gratitude towards the faculty members of the Department of Physics (SPAS) at Goa University for their continuous support and for creating a stimulating learning environment. I would like to thank the School of Physics and Applied Sciences for providing me with all the required instruments for my project work.

Next, I want to acknowledge all the PhD students in the Physics department who have assisted me by explaining how to use different instruments and software. I am also grateful to my family and friends for their unwavering support and encouragement throughout my studies.

Table of Contents

Acknowledgement.....	i
Table of Figures.....	iv
Abstract.....	vi
1. INTRODUCTION.....	1
1.1 Perovskites	1
1.2 Halide Perovskites.....	3
1.3 Properties.....	4
1.3.1 Structural.....	4
1.3.2 Optoelectronic	6
1.4 Applications	7
1.4.1 Solar cell.....	7
1.4.2 Light emitting diodes (LEDs).....	8
1.4.3 Photodetectors	9
1.5 Effect of Pb based halide perovskites	10
1.6 Sn based halide perovskites.....	11
1.7 References	12
2. LITERATURE REVIEW.....	14
2.1 References	19
3. METHODS OF PREPARATION	21
3.1 Mechanochemical synthesis	21

3.2 Thermal Annealing	22
3.3 Hot Injection.....	23
3.4 Hydrothermal/Solvothermal method	24
3.5 Sonochemical method	26
3.6 Ligand assisted reprecipitation (LARP)	26
3.6.1 Synthesis of CsPb _{1-x} Sn _x Cl ₃	27
3.7 References.....	29
4. CHARACTERIZATION TECHNIQUES	31
4.1 X-ray diffraction (XRD).....	31
4.2 UV-Visible Spectroscopy.....	33
4.3 Photoluminescence (PL) Spectroscopy.....	34
4.4 Raman Spectroscopy.....	37
4.5 Scanning Electron Microscopy (SEM)	38
4.6 References.....	41
5. RESULTS.....	43
5.1 X-ray Diffraction.....	43
5.2 UV-Visible Spectroscopy.....	45
5.3 Photoluminescence spectroscopy	51
5.4 Scanning electron microscopy.....	54
5.5 Raman spectroscopy	55
5.6 References.....	59
6. CONCLUSION	62

Table of Figures

Figure 1 Typical perovskite cubic structure with the BO_6 octahedra. (3)	1
Figure 2 Perovskite ABX_3 lattice. (a) Large A and small B cations, with X anions; (b) octahedron by X anions; (c) octahedra lattice. (4).....	2
Figure 3 General structures of (a) inorganic perovskites and (b) hybrid perovskite. (9)	3
.Figure 4 Ideal cubic halide perovskite structure of ABX_3 . (a) Unit cell; (b) coordination of A site and; (c) coordination of B site	4
Figure 5 Different unit cells of perovskite based on tolerance factor. (12).....	5
Figure 6 Architecture of perovskite solar cell device. (13).....	8
Figure 7 PeLED device architecture. (13)	9
Figure 8 Device structure of photodetector (7)	10
Figure 9 Schematic diagram of Mechanochemical synthesis (1).....	21
Figure 10 Schematic diagram of hot injection method (5)	24
Figure 11 CsPbX_3 synthesis using hydrothermal method from precursor dispersion (6).....	25
Figure 12 Schematic diagram of sonochemical method. (1).....	26
Figure 13 Schematic diagram for LARP synthesis method. (8).....	27
Figure 14 Steps involved in the synthesis of the $\text{CsPb}_{1-x}\text{Sn}_x\text{Cl}_3$ samples.....	28
Figure 15 schematic diagram of Bragg's Law, (3)	31
Figure 16 Schematic diagram of components of XRD diffractometer. (4).....	32
Figure 17 Diffractometer used in the dissertation.....	32
Figure 18 Schematic diagram of Uv-Vis spectrometer. (5).....	33
Figure 19 Schematic diagram of a photoluminescence setup. (7)	36
Figure 20 schematic diagram of Raman spectroscopy instrument. (10).....	38
Figure 21 Schematic diagram of a scanning electron microscope. (12)	40
Figure 22 Rietveld refined patterns of $\text{CsPb}_{1-x}\text{Sn}_x\text{Cl}_3$ ($x = 0, 0.25, 0.5, 0.75$) and Cs_2SnCl_6	44

Figure 23 UV-Vis spectroscopy setup for powder sample	45
Figure 24 Absorption spectra of $\text{CsPb}_{1-x}\text{Sn}_x\text{Cl}_3$ ($X = 0, 0.25, 0.5, 0.75$) and Cs_2SnCl_6	46
Figure 25 Tauc plots of $(\alpha h\nu)^2$ v/s energy for $\text{CsPb}_{1-x}\text{Sn}_x\text{Cl}_3$ and Cs_2SnCl_6	48
Figure 26 Absorption spectras for $\text{CsPb}_{1-x}\text{Sn}_x\text{Cl}_3$ ($x=0, 0.25, 0.5, 0.75$) and Cs_2SnCl_6	50
Figure 27 PL spectrum of $\text{CsPb}_{1-x}\text{Sn}_x\text{Cl}_3$ and Cs_2SnCl_6	51
Figure 28 PL spectrum of $\text{CsPb}_{1-x}\text{Sn}_x\text{Cl}_3$ ($x=0, 0.25, 0.5, 0.75$) and Cs_2SnCl_6	53
Figure 29 SEM images of CsPbCl_3 at $10\mu\text{m}$ and 200 nm	54
Figure 30 SEM images of $\text{CsPb}_{0.75}\text{Sn}_{0.25}\text{Cl}_3$	54
Figure 31 SEM images of $\text{CsPb}_{0.5}\text{Sn}_{0.5}\text{Cl}_3$	54
Figure 32 SEM images of $\text{CsPb}_{0.25}\text{Sn}_{0.75}\text{Cl}_3$	55
Figure 33 SEM images of Cs_2SnCl_6	55
Figure 34 Instrument used for acquiring raman spectra.....	56
Figure 35 Raman spectra of prepared samples.	56
Figure 36 Raman spectras of $\text{CsPb}_{1-x}\text{Sn}_x\text{Cl}_3$ ($x=0, 0.25, 0.5, 0.75$) and Cs_2SnCl_6	58

ABSTRACT

Lead based perovskites have become extremely popular in the photovoltaic devices applications, due to their high power conversion efficiencies and low manufacturing costs. However, lead being a toxic material hinders their large scale commercial application. Recently, tin-based perovskites have started to become a very good candidate to substitute the lead halide perovskites as they have a bandgap near the optimal value for PV applications and even showed similar or even better optical and electronic properties compared to lead based perovskites. They also have a strong optical absorption and good charge carrier mobility. The synthesis of $\text{CsPb}_{1-x}\text{Sn}_x\text{Cl}_3$ was done by employing the ligand-assisted reprecipitation (LARP) method at room temperature. All $\text{CsPb}_{1-x}\text{Sn}_x\text{Cl}_3$ crystallized in cubic phase with $Pm\bar{3}m$ spacegroup, while CsSnCl_3 couldn't be synthesized, Cs_2SnCl_6 had been formed which crystallized in cubic phase with $Fm\bar{3}m$ spacegroup. The absorption and emission peak shifted to slightly longer wavelengths with increasing Sn content while, the bandgap decreased. Scanning electron microscope (SEM) images revealed uniform cubic morphology of the samples with octahedron morphology for the Cs_2SnCl_6 . Both $\text{CsPb}_{1-x}\text{Sn}_x\text{Cl}_3$ and Cs_2SnCl_6 had three raman active modes. Further research is required for finding the optimal antisolvent and temperature for synthesizing CsSnCl_3 .

1. INTRODUCTION

1.1 Perovskites

Perovskite is originally CaTiO_3 mineral, which was discovered by Gustav Rose (Prussian mineralogist) in 1839 in the Ural mountains and named after Count Levi Aleksevich von Petrovski (Russian mineralogist). (1) But presently, Perovskites are a family of compounds with a general formula of ABO_3 (A= cation, B= anion, O= oxide).

Most naturally occurring perovskites are oxide based corner-sharing BO_6 octahedra crystallizing in the ABO_3 structure. Perovskites are ideally considered to have a cubic structure, however, ironically the first discovered perovskite actually had a orthorhombic structure. The ideal cubic structure has a $Pm\bar{3}m$ space-group but, most of the perovskites develop a reduced symmetry owing to lattice distortions, distorted octahedra, ordered cations, vacancies, or the presence of organic or inorganic cations.

There are many different classes of perovskites such as metallic perovskites, organic perovskites, inorganic perovskites, complex organic-inorganic perovskites, halide perovskites etc. There even exist noble gas perovskites indicating perovskite structure crystal lattice being highly adaptable. (2)

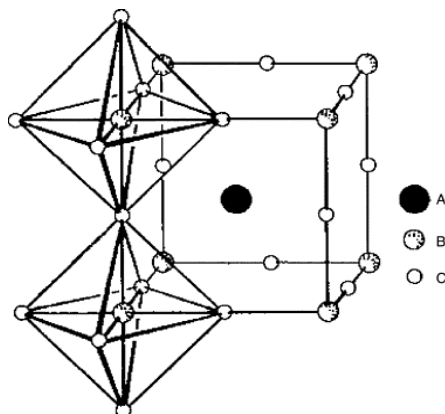


Figure 1 Typical perovskite cubic structure with the BO_6 octahedra. (3)

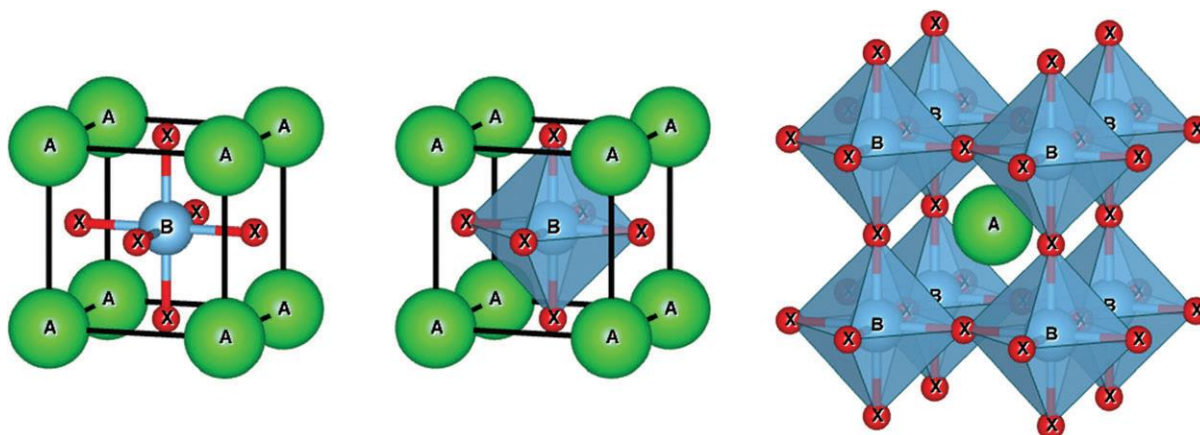


Figure 2 Perovskite ABX_3 lattice. (a) Large A and small B cations, with X anions; (b) octahedron by X anions; (c) octahedra lattice. (4)

Perovskites exhibit magnetic properties as they have incompletely filled d - or f -block elements at A or B sites as many perovskites have transition metal (d -block) and lanthanides (f -block) elements at these A and B sites. Perovskites show magnetic behaviour because of the spin states of cations and magnetic moments. At high temperatures paramagnetic behaviour is observed due to disorders from temperature dependent magnetic susceptibility, but, at lower temperatures due to interaction of magnetic moments we can see antiferromagnetic, ferromagnetic and ferrimagnetic behaviour. (5)

Perovskite properties are mostly governed by the cation at the B site due to their d -electron configuration. Electronic properties like metallic, semiconducting, superconducting, insulating, piezoelectric, thermoelectric, etc. are shown by perovskites. These properties can be varied by changing the crystal structure, phase transformations, vacancies in A, B or O sites and are also temperature dependent. Electronic conduction in perovskite is caused by the action of several electron interactions. Insulating perovskites show dielectric, ferroelectric and piezoelectric properties whereas the conducting perovskites show thermoelectric properties. For example, $BaTiO_3$ is an insulator at room temperature owing to its closed-shell configuration, but below Curie temperature (120°C) shows ferroelectric behaviour and above

curie temperature shows paraelectric behaviour due to phase transition from Tetragonal to cubic phase where it loses the spontaneous dipoles. (6,7).

1.2 Halide Perovskites

As seen earlier there are many different classes of perovskites but we will majorly discuss halide Perovskites owing to their wide scale range of applications in optical and optoelectronic fields. In Halide perovskites the O anion from the ABO_3 structure is replaced by X halide thus the structure is written as ABX_3 ($x= Cl^-, Br^-, I^-$). Here also, the ideal structure is cubic with $Pm\bar{3}m$ Space-group. In the standard ABX_3 Perovskites the A cation is a large monovalent alkali metal such as Caesium (Cs), or organic cations such as methylammonium or formamidinium, the B cations are divalent such as Pb, Mn, Sn etc. The two categories of halide perovskites for our study are the inorganic halide perovskites and organic-inorganic hybrid perovskites. In the inorganic perovskites either the A or B site is occupied by organic ions, typically it the A site is occupied by organic ion and B site by a metal. The most common A site organic ions being methylammonium or formamidinium. (2,8)

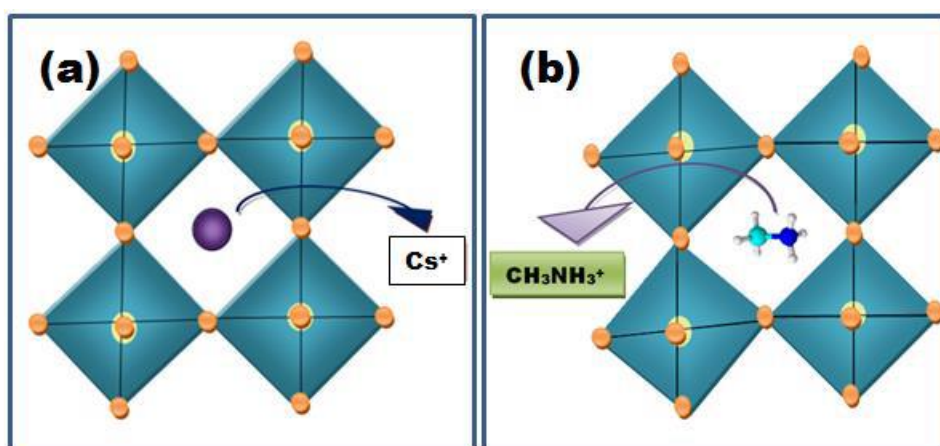


Figure 3 General structures of (a) inorganic perovskites and (b) hybrid perovskite. (9)

1.3 Properties

1.3.1 Structural

The ideal structure of inorganic halide perovskites is again a cubic structure (Figure 4a) with $Pm\bar{3}m$ space-group. (10)

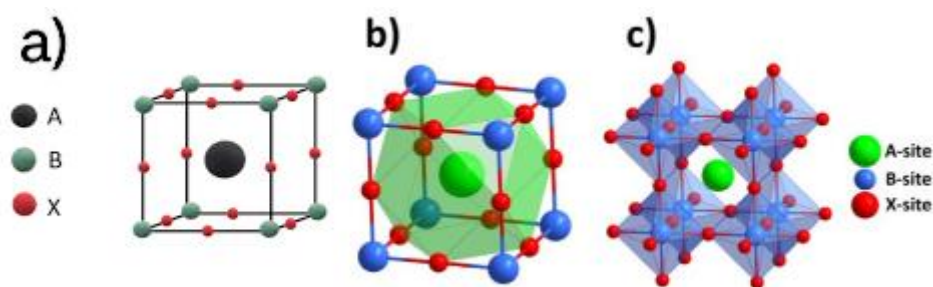


Figure 4 Ideal cubic halide perovskite structure of ABX_3 . (a) Unit cell; (b) coordination of A site and; (c) coordination of B site

In the cubic ABX_3 halide perovskite A-site cation has a 12-fold coordination and occupies body-centred position while the B-site cation has a 6-fold coordination at is placed at the corners. X halide is located at centres of the 12 edges. A-site has a cuboctahedral shape with coordination number of 12 (Figure 4b). The unit cell consists a network of corner sharing BX_6 octahedra with linear X-B-X bonds. Deviations from the ideal cubic structure are caused by the difference in the sizes of A- and B-site cations. (10) The A-site cation is responsible for filling the void between connected octahedral and neutralizing charges of octahedron network. (9) Perovskite stability is predicted by Goldschmidt tolerance factor given as :

$$t = \frac{r_A + r_X}{\sqrt{2}(r_B + r_X)}$$

r_A , r_B , r_X refer to the ionic radii of A, B and X ions

Stable perovskites structures are formed for t value between 0.78-1.13, as a result only cations such as Cs, methylammonium and Formamidinium can produce structurally stable halide perovskites. (11) As t value approaches 1 the halide perovskite structure tends to be cubic, a rough estimate for structures based on t values is as follows: $1 < t < 1.13$, the structure is hexagonal; $0.9 < t < 1$, gives cubic structure; $0.75 < t < 0.9$; results in a orthorhombic structure. Generally, the two conditions for perovskite formation is the (i) electroneutrality-perovskite formula with neutral balanced charge; and (ii) Ionic Radii should be $r_A > 0.09$ nm and $r_B > 0.051$ nm, with t values between 0.8 and 1. (12)

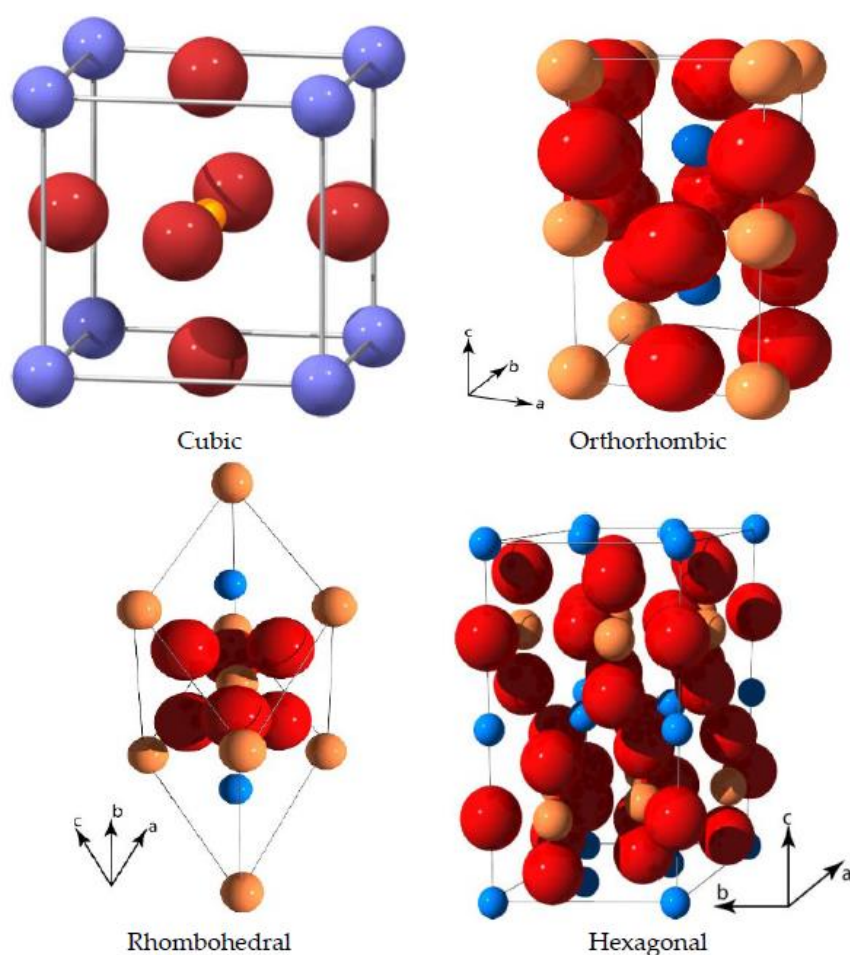


Figure 5 Different unit cells of perovskite based on tolerance factor. (12)

1.3.2 Optoelectronic

Halide perovskites in general have a very large absorption coefficient, Its optical energy bandgap can be varied and tuned easily over a range of wavelength by changing the composition of A B and X ions and also external parameters like pressure and temperature, more importantly, they show emission throughout the visible range. Halide perovskites also have a high quantum efficiency with quantum confinement effect. Halide perovskites show a very good PLQY of 20%. (11)

Emission wavelength of CsPbX_3 ($X = \text{Cl}, \text{Br}, \text{and I}$) nanocrystals can be varied from 410 nm to 685 nm just by varying X. This is due to the electronic structure of halide perovskites. Halide P-orbitals and metal S-orbitals mix to form the perovskite Valence Band Minimum (VBM). On changing the halide from Cl^- to Br^- , there is an increase in the halogen p-character in the VBM, due to this the spin orbit coupling increases, as a result the bandgap decreases along with a red shift in PL spectrum on changing the halide from Cl^- to Br^- . When there is a phase transition in the crystal structure from cubic to tetragonal or other phases causes octahedral tilt (due to decreased Pb-X-Pb dihedral angle by replacing a large A-site ion to a smaller one such as Cs^+), the bandgap increases with a blueshift in PL as a result of weakened spin orbit coupling. (13,11)

Decrease in A size ion decreases the bandgap (blueshift) due to increased Pb-X-Pb tilting angle as the cubic crystal structure distorts. Similarly, B and X ions also affects the optical properties of metal halide perovskites, for example, substituting Sn^{2+} in place of Pb^{2+} in the B-site results in increased Photoluminescence and decreased bandgap. (13)

Crystalline size also governs the optoelectronic properties. We can also have a halide perovskite with a narrow PL bands, blueshifted absorption and PL spectra by lowering the size below exciton Bohr radius, this effectively causes quantum confinement in perovskites.

Changes in temperature causes phase transitions and thermal expansion varies the exciton-phonon interactions. In general, the stabilized cubic phase in Halide perovskites is formed at a high temperature. This results in minimal octahedral tilt and strong spin orbit coupling, causing the bandgap to decrease with a redshift in absorption and PL spectra.

Doping the metal halide perovskite at B-site can also affect the emission due to additional ions which might result in strongly Stoke-shifted emission and can also result is dual emission wavelengths. The blueshift after alloying (adding dopants like Mn^{2+} in place of Pb ions) is due to lattice contraction, which also widens the bandgap. Perovskite nanocrystals act as a host for exciting dopants through energy transfer. (11)

1.4 Applications

1.4.1 Solar cell

The basic principle of a solar cell is the absorption of sunlight and then the creation of potential difference between two electrodes to generate electricity, this is called photovoltaic effect.

Perovskites are becoming very popular as a material for solar cells owing to their high absorption coefficient, long diffusion lengths of charge carriers, defect tolerance and low exciton energies. Perovskite is used as an active layer for charge transfer in solar cells. Quality of perovskite layer and defect-free interfacial structure play a very important role in deciding the efficiency of perovskite solar cells (PSCs). PSCs offer a very good power conversion efficiency close to the commercially available solar cells and their device fabrication is also cost effective. (13)

In the architecture of PSCs, perovskite layer acts as a intrinsic light absorber (As showed in Figure 5) sandwiched between the electron-transport layer (ETL) and the hole-transport layer (HTL) on a substrate made of fluorine-doped tin oxide (FTO) or ITO. (13)

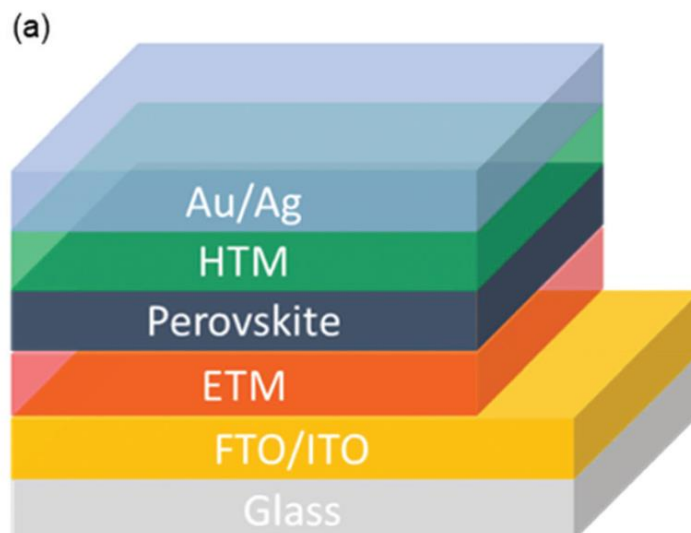


Figure 6 Architecture of perovskite solar cell device. (13)

After the absorption of light by perovskite layer the photogenerated electrons are transferred to the conduction band of ETL and then to FTO/ITO. Holes get transferred to the valence band due to the HTL and then to the Au/AG layer. One great advantage of using perovskite is that the charge carriers can be extracted even in the absence of ETL or HTL. This is because of the low exciton binding energy and the ambipolar charge carrier mobility of perovskites which results in a p-i-n or a n-i-p junction being formed in a PSC. (13)

1.4.2 Light emitting diodes (LEDs)

Perovskites have gained considerable attraction in the fabrication of multicolour LEDs, these are called Perovskite LEDs (PeLEDs), due to their tuneable PL and high PLQY. Perovskite materials have low defect density and ambipolar carrier migration which results in efficient injection and transport of charges across interfaces causing enhanced device performance.

In the PeLED device structure, halide perovskite is used as a light emitting layer in between the charge(electron and hole)-injection (transfer) layers and electrodes. The charge-injection layers are large bandgap semiconductors enabling efficient and balanced injection and charge confinement of carriers. The configuration of PeLED is shown in Figure 6

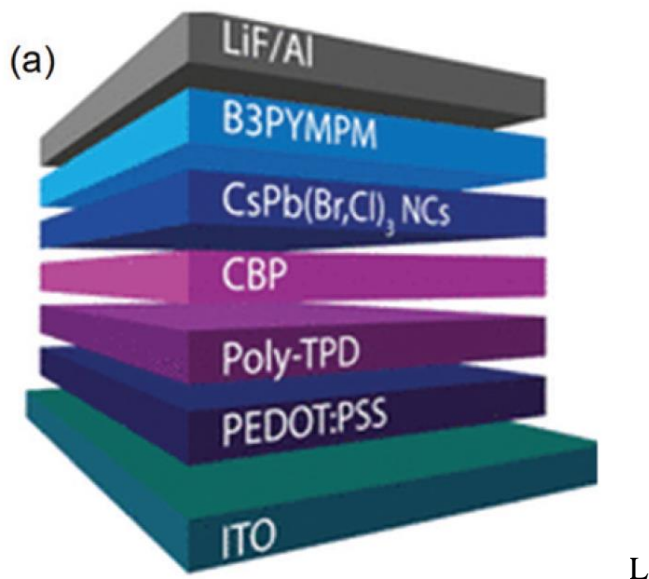


Figure 7 PeLED device architecture. (13)

Crystal structure, atmosphere, temperature and light affects the stability of halide perovskites and the efficiency of PeLEDs. Other factors influencing the performance of PeLEDs include unbalanced charge-injection and transport across perovskite/electron layer or perovskite/hole layer. Leakage current can be increases by increasing the surface coverage and reducing surface roughness of perovskite layer. (13)

1.4.3 Photodetectors

Photodetectors convert optical signal into electrical-photon energy to current or voltage output. Halide perovskite photodetectors can transduce photons of different enerhies according to their bandgap. Although Ge, graphene, Si, ZnO and their heterojunctions based photodetectors have been well established, but these photodetectors require high-temperature manufacturing process and their device structures are complex. Hence, it is essential to find photodetectors have low-cost, simple device structure and high-performance. CsPbX₃ based photodetectors consist of heavily doped Si or ITO/polyethylene terephthalate (PET) as the substrate and pre-patterned gold/aluminium/silver electrode. CsPbX₃ acts as the active layer. CsPbI₃ thin film based photodetector gives good on/off photocurrent ratio, and also the rise

and decay times observed are 24 and 29 ms, respectively. CsPbBr₃ and CsPbI₃ based photodetectors have a maximum response at the wavelengths of 517 and 630 nm, which are in agreement with the maximum absorption peaks of CsPbBr₃ NC and CsPbI₃ nanosheets, respectively. (13)

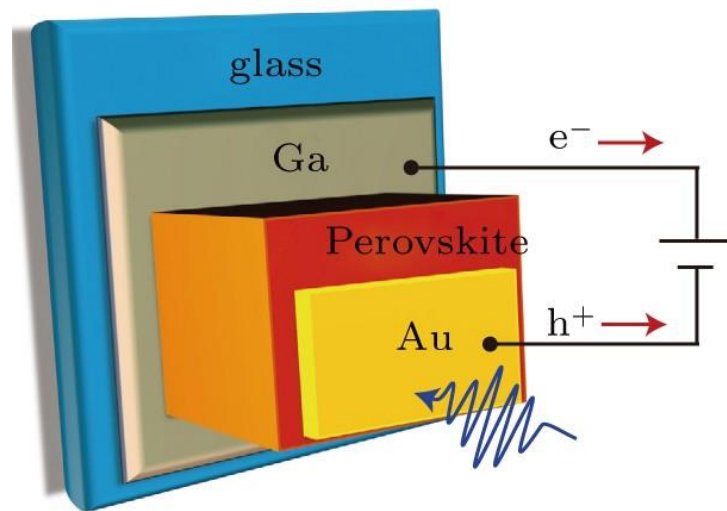


Figure 8 Device structure of photodetector (7)

1.5 Effect of Pb based halide perovskites

Lead based perovskites have become extremely popular in the photovoltaic devices applications, mainly as an alternative to the commercially available silicon-based solar cells due to their high cost and complex fabrication procedures. This is because lead halide perovskites have high power conversion efficiencies and low manufacturing costs. They also have a narrow emission half width, high charge carrier mobility and long lifetime of minority carriers which make them promising emitting materials for luminescence and display applications. (14,15)

However, lead being a toxic material to the environment as well as human health hinders their large scale commercial application. Apart from toxicity, lead halide perovskite's solubility in water causes poor long-term stability. (14)

1.6 Sn based halide perovskites

Due to the toxicity of lead, there has been great research for finding a lead free alternative for perovskite's photovoltaic application. Now, tin-based perovskites are found to be a very good candidate to substitute the lead halide perovskites. Tin halide perovskites have a bandgap near the optimal value for PV applications. Sn-based perovskites have even showed similar or even better optical and electronic properties compared to lead based perovskites. They also have a strong optical absorption and good charge carrier mobility. Theoretically, these Sn perovskites can even achieve power conversion efficiency around 33%. Currently, researchers are trying to improve the defect tolerance and instability of Sn based halide perovskites. (15,16)

1.7 References

1. Iniewski K&NW&HY&SM. Perovskite Materials: Application Perspective. Metal-Halide Perovskite Semiconductors: From Physical Properties to Opto-electronic Devices and X-ray Sensors. 2023;(2023): 1-16.
2. Akkerman QAaML. What Defines a Halide Perovskite? ACS Energy Letters. 2020; 5: 604-610.
3. L.Q. Jiang JKGHBLMZXZPWCHL. Prediction of lattice constant in cubic perovskites. Journal of Physics and Chemistry of Solids. 2006; 67(7): 1531-1536.
4. Gibin George SREZL. Introduction to Perovskites. In Fundamentals of Perovskite Oxides.; 2020. p. 2.
5. Gibin George SREZL. Magnetic properties of Perovskite Oxides. In Fundamentals of Perovskite Oxides Synthesis, Structure, Properties and Applications.; 2020. p. 155.
6. Gibin George SREZL. Electronic Properties of Perovskite Oxides. In Fundamentals of Perovskite Oxides Synthesis, Structure, Properties and Applications.; 2020. p. 185.
7. Cambridge Uo. Dissemination of IT for the Promotion of Materials Science (DoITPoMS). [Online]. Available from:
https://www.doitpoms.ac.uk/tlplib/ferroelectrics/phase_changes.php.
8. F. Sunny LMVNKaKBS. Metal Halide Hybrid Perovskites. In Recent Advances in Multifunctional Perovskite Materials.; 2022.
9. Muhammad A. SYNTHESIS OF METAL HALIDE PEROVSKITE MATERIALS FOR

LIGHT HARVESTING APPLICATIONS. ; 2018.

10. Gibin George SREZL. Crystal Structure of Simple Perovskites. In *Fundamentals of Perovskite Oxides Synthesis, Structure, Properties and Applications.*; 2020. p. 87-88.
11. Javad Shamsi ASUMILDTaLM. Metal Halide Perovskite Nanocrystals: Synthesis, Post-Synthesis Modifications, and Their Optical Properties. *Chemical Reviews.* 2019; 119(5): 3296-3348.
12. Atta NF GAEAE. Perovskite Nanomaterials – Synthesis, Characterization, and Applications. In *Perovskite Materials.*: IntechOpen; 2016. p. 109-111.
13. Lata Chouhan SGCSTMaVB. Synthesis, optoelectronic properties and applications of halide perovskites. *Chem Soc Rev.* 2020; 49(10): 2869-2885.
14. Pitaro Matteo TKESSaLAM. Tin Halide Perovskites: From Fundamental Properties to Solar Celss. *Advanced Materials.* 2022 January; 34(1): 2105844.
15. Jianing Cheng YL,WQ,MS,YL,WS,WDYZ. Mechanochemical synthesis and characterization of Mn-doped CsPbCl₃ perovskite nanocrystals. *Journal of Alloys and Compounds.* 2020; 822: 153615.
16. Tom C. Jellicoe JMR,HFJGMTRBSED,RARHF,DC,NCG,aMLB. Synthesis and Optical Properties of Lead-Free Cesium Tin Halide perovskite Nanocrystals. *Journal of the American Chemical Society.* 2016; 139(9): 2941-2944.

2. LITERATURE REVIEW

Tom et.al synthesized CsSnX_3 ($X = \text{Cl, Br, I, Cl}_{0.5}, \text{Br}_{0.5}, \text{I}_{0.5}$) using hot injection method and their optical properties were studied. They found that CsSnCl_3 crystallized in a cubic structure with the lattice parameters of 5.57 \AA , while CsSnBr_3 crystallized in a orthorhombic structure with lattice parameters of $a=8.21 \text{ \AA}$, $b=11.63 \text{ \AA}$ and $c=8.18 \text{ \AA}$ and CsSnI_3 also crystallized in orthorhombic structure with lattice parameters of $a=8.69 \text{ \AA}$, $b=12.37 \text{ \AA}$, $c=8.63 \text{ \AA}$. From UV-Vis and PL studies they found that the bandgap has a redshift and they gave the reason for this redshift to be the high electronegativity of Sn^+ . They also found that these materials exhibited quantum confinement effect. They have found that the optical bandgap can be changed throughout the near-infrared and visible region by changing X anion and also by varying the synthesis temperature. (1)

Chen et.al synthesized CsPbX_3 ($X = \text{Cl, Br, I, and mixed Br/Cl, Br/I}$) using solvothermal synthesis. XRD analysis revealed that all CsPbX_3 nanocrystals formed cubic phases. They found that the prepared CsPbBr_3 nanowires showed orthorhombic phases. They also found that CsPbBr_3 undergoes phase transitions from cubic phase at 140° to mixed cubic and orthorhombic phases at 180° . UV-Vis and PL spectroscopy showed emission of CsPbX_3 can be tuned over the entire visible range by adjusting the compositions of anions. CsPbCl_3 showed a sharp absorption peak at 400 nm and bright purple emission with emission peak at 410 nm , while CsPbBr_3 shows absorption peak at 510 nm and strong green emission with emission peak at 520 nm and CsPbI_3 showed absorption peak at around 680 nm and red emission with emission peak around 700 nm . They also concluded that choosing Caesium precursor is important as it determines the morphology and quality of the formed materials. (2)

Wei Zhai et.al prepared CsPbX₃ (X= Cl, Br) nanocrystals via solvothermal synthesis and also they fabricated CsPbX₃ based photodetectors where in SiO₂/Si wafers were cleaned via sonication followed by treating the wafers using Uv-ozone cleaners and after that the CsPbX₃ nanowires dissolved n-hexane solution were dropped onto the SiO₂/Si wafers and dried at room temperature. CsPbX₃ crystallized in cubic phase. The nanowires formed were homogenous with high purity and high yield, which are suitable for large scale applications. The nanowires agglomerated together and showed good flexibility. CsPbBr₃ exhibited fluorescence characteristics. They found the length of nanowires to be 10 microns. High resolution TEM and Fourier transform patterns showed the growth along [100] direction. Uv-Vis spectroscopy showed absorption peak for CsPbCl₃ at 405 nm while, CsPbBr₃ showed absorption peak at around 510 nm. The PL spectra showed that CsPbCl₃ has a emission peak at 410 nm and CsPbBr₃ at 520 nm. The bandgap was found to be 3.02 eV and 2.38 eV for CsPbCl₃ and CsPbBr₃ respectively. (3)

Hua-Rong Xia et.al synthesized CH₃NH₃PbBr₃ and CH₃NH₃PbI₃ for Li-ion battery applications using hydrothermal method. XRD analysis showed that CH₃NH₃PbBr₃ had a cubic (*Pm $\bar{3}$ m*) structure with lattice parameter of 5.9394 Å and CH₃NH₃PbI₃ had a tetragonal (*I4/mcm*) structure with lattice parameters of a=8.8048 Å and b=12.7411 Å. SEM images of CH₃NH₃PbBr₃ showed hierarchical rod like structures with a particle size of ~100 µm. SEM images of CH₃NH₃PbI₃ showed clusters of micrometre sized wires with a diameter of tens of microns and length of hundreds of microns. EDX studies confirmed the elemental composition of Pb²⁺ and Br⁻. The fabricated Li-ion batteries of CH₃NH₃PbBr₃ and CH₃NH₃PbI₃ had a first discharge capacity of 331.8 mAh/g and 43.6 mAh/g while, the 15th discharge capacity of CH₃NH₃PbBr₃ was 175.5 mAh/g which was found to be equivalent to commercial Li₄Ti₅O₁₂. They found that CH₃NH₃PbBr₃ had a greater performance than CH₃NH₃PbI₃ and concluded that composition of perovskites played an important role. (4)

Bharat R. Bade et.al synthesized Formamidinium Lead Iodide (FAPbI₃) perovskite using one step low temperature chemical synthesis and a FAPbI₃ thin film using spin coating and aimed to produce for a low-cost absorber in solar cells. XRD analysis showed FAPbI₃ crystallized in a cubic structure with diffraction peaks at 13.70, 19.8°, 26°, 28.3°, 31.5°, 34.1°, 39.7°, 42.9°, 45.1°, 47.9°, 50.4°, 52.4°, and 56.7° corresponding to (100), (110), (111), (002), (210), (220), (221), (310), (113), (222), (320), (321) and (004) planes. They found that δ -FAPbI₃ was not formed and confirmed that high quality α -FAPbI₃ had been synthesized. The crystalline size was found to be 40 nm and the interplanar spacing was found to be 6.38 Å. Uv-Vis spectroscopy showed the absorption peak at 900 nm and the bandgap was found to be 1.55 eV. PL spectroscopy showed emission between 710-740 nm with emission peak at 727 nm confirming the presence of most stable α phase. TEM imaging showed the presence of particles with differently oriented crystallites. Interplanar distance was found to be 0.657 nm which was very close to the one obtained from XRD. They concluded that FAPbI₃ perovskite synthesized by a simple low-temperature chemical technique is a better candidate for applications in optoelectronic and photovoltaic device applications. (5)

Jianing Cheng et.al synthesized Mn doped CsPbCl₃ perovskite using mechanochemical synthesis and its structural and optical properties were studied. XRD analysis showed that the undoped CsPbCl₃ had cubic phase with the lattice parameter of 5.605 Å. With Mn/(Mn+Pb) doping ratio between 0.03 and 0.15 the (101) peak shifted to higher 2 θ with increase in Mn content. The reason for this shift was that the ionic radius of Mn²⁺ is 0.97 Å which is less than the ionic radius of Pb²⁺ and this suggested that Mn was incorporated in CsPbCl₃ NCs. When the Mn ratio was greater than 0.20, diffraction peaks not attributing to CsPbCl₃ appeared and the intensity of (101) and (200) peak became weak. For Mn/(Mn+Pb) ratio greater than 0.40 irregular diffraction peaks occurred which pointed towards the collapse of host CsPbCl₃ and the formed CsMnCl₃ had a trigonal phase, indicating a phase transition

from cubic to trigonal structure as a result of Mn doping. TEM imaging showed that the undoped CsPbCl₃ NCs had a cubic shape with average size of 13 nm. HR-TEM for undoped sample showed that the NCs had a high crystallinity with d-spacing of 0.39 nm, which is for the (101) cubic plane of perovskite crystal. For Mn doping ratio between 0.03 and 0.10 the crystal's shape and sizes were identical to the undoped sample. Uv-Vis spectroscopy showed that the undoped CsPbCl₃ had a absorption peak at 400 nm. As the doping content of Mn increased, a blue shift was observed in the absorption peak due to existence of secondary phases. For Mn ratio greater than 0.6 there was no absorption peak indicating the collapse of host CsPbCl₃. The bandgap of CsPbCl₃ was 3.02 eV which was same as the undoped sample. PL spectroscopy showed that the undoped sample had only one emission peak at 412 nm. While Mn doped samples had two emission peaks at 412 nm and broad emission peak near 594 nm. Mn doping caused the emission to shift to long wavelength. (6)

Valdi Rizki Yandri et.al synthesized CsPbCl₃ and CsPbBr₃ using LARP method. They found that changing the reaction temperature can be used to vary the size of CsPbX₃. XRD analysis showed that both CsPbCl₃ and CsPbBr₃ have a cubic phase, The lattice parameters of CsPbCl₃ and CsPbBr₃ were 5.61 Å and 5.83 Å respectively. They found that these lattice parameters are same as the ones from hot injection and mechanochemical method. PL spectroscopy for CsPbCl₃ showed emission peak at 435 nm and CsPbBr₃ at around 516-527 nm. They found that PL characteristics of CsPbCl₃ show band tail characteristics, which may have been originated from disordered or defect states on the CsPbCl₃ NC surfaces. (7)

Carlos et.al prepared CsPbX₃ (X = Cl, Br and I) using hydrothermal method. Raman spectroscopy showed four Raman active modes for both CsPbCl₃ and CsPbBr₃ while pure CsPbI₃ had only two Raman active modes. CsPbCl₃ has a cubic phase while CsPbBr₃ and δ -CsPbI₃ had orthorhombic phase. They found that cubic CsPbCl₃ and orthorhombic CsPbBr₃ have direct bandgap, CsPbI₃ has indirect bandgap. CsPbCl₃, CsPbBr₃ and CsPbI₃ have a

bandgap values of 2.6 eV, 2.14 eV and 2.56 eV respectively. They found that the defect states play a major role in optical and electronic response of CsPbX₃ perovskite structure. (8)

Tong Cai et.al synthesized Cd-doped CsPbCl₃ using colloidal synthesis. PL spectroscopy showed emission peak at around 420 nm, while the Cd-doped CsPbCl₃ NCs showed another emission band at 610 nm and with maximal PLQY of about 8%. They found that PL Excitation spectrum matched well with absorption profile, as a result the emission band was due to the energy transfer process from host NCs to Cd-doped NCs. They found that Cd-doped NC's bandgap (BG) emission peak was blue-shifted with enlarged stokes shift when compared with undoped NCs, indicating an alloying effect accompanied by lattice contraction on adding Cd-dopants. SAED indicates cubic symmetry. PL lifetime measurement revealed that average lifetime of BG-PL decreased dramatically when Cd-doping increased. (9)

2.1 References

1. Jellicoe TC, Richter JM, Glass HF, Tabachnyk M, Brady R, Dutton SE, Rao A, Friend RH, Credginton D, Greenham NC, Böhm ML. Synthesis and optical properties of lead-free cesium tin halide perovskite nanocrystals. *Journal of the American Chemical Society*. 2016 Mar 9;138(9):2941-4.
2. Chen M, Zou Y, Wu L, Pan Q, Yang D, Hu H, Tan Y, Zhong Q, Xu Y, Liu H, Sun B. Solvothermal synthesis of high-quality all-inorganic cesium lead halide perovskite nanocrystals: from nanocube to ultrathin nanowire. *Advanced Functional Materials*. 2017 Jun;27(23):1701121.
3. Zhai W, Lin J, Li C, Hu S, Huang Y, Yu C, Wen Z, Liu Z, Fang Y, Tang C. Solvothermal synthesis of cesium lead halide perovskite nanowires with ultra-high aspect ratios for high-performance photodetectors. *Nanoscale*. 2018;10(45):21451-8.
4. Xia HR, Sun WT, Peng LM. Hydrothermal synthesis of organometal halide perovskites for Li-ion batteries. *Chemical communications*. 2015;51(72):13787-90.
5. Bade BR, Rondiya SR, Kore KB, Nilegave DS, Nasane MP, Jathar SB, Barma SV, Funde AM. Room temperature synthesis of formamidinium lead iodide (FAPbI₃) perovskite for low-cost absorber in solar cells. *ES Energy & Environment*. 2021 May 4;13:31-6.
6. Jianing Cheng YL,WQ,MS,YL,WS,WDYZ. Mechanochemical synthesis and characterization of Mn-doped CsPbCl₃ perovskite nanocrystals. *Journal of Alloys and Compounds*. 2020; 822: 153615.
7. Yandri VR, Wulandari P, Hidayat R. Photoluminescence Properties of CsPbCl₃ and CsPbBr₃ Nanocrystals synthesized by LARP Method with Various Ligands and Anti-solvents. In *Journal of Physics: Conference Series* 2022 Jun 1 (Vol. 2243, No. 1, p. 012120). IOP Publishing.

8. Echeverría-Arrondo C, Alvarez AO, Masi S, Fabregat-Santiago F, Porta FA. Electronic, Structural, Optical, and Electrical Properties of CsPbX₃ Powders (X= Cl, Br, and I) Prepared Using a Surfactant-Free Hydrothermal Approach. *Nanomanufacturing*. 2023 May 19;3(2):217-27.
9. Cai T, Yang H, Hills-Kimball K, Song JP, Zhu H, Hofman E, Zheng W, Rubenstein BM, Chen O. Synthesis of all-inorganic Cd-doped CsPbCl₃ perovskite nanocrystals with dual-wavelength emission. *The Journal of Physical Chemistry Letters*. 2018 Dec 4;9(24):7079-84.

3. METHODS OF PREPARATION

3.1 Mechanochemical synthesis

Mechanochemical synthesis is based on the principle where mechanochemical forces on reactants results in the formation of the target material in powder form. It is one of the simplest methods for formation of perovskite NCs. In this method individual precursor powders, e.g., CsCl and PbCl₂ are grinded together with a mortar and pestle until there is a colour change indicating the formation of perovskite. A better and controlled way to form perovskite by this method is by using ball mills such as shaker mills, or planetary ball mills. In this milling method the precursor powders are weighed in the desired stoichiometry and then put into the milling jars along with the milling balls. Stainless steel or toughened zirconia is usually used to make these balls and milling jars. Sometimes a liquid grinding agent (e.g., cyclohexane) maybe added which results in a modified method called wet ball milling (liquid assisted grinding). After adding precursors and balls the milling jars, the jars are tightly closed, and then the jar is put into the mill and the start of synthesis process is indicated by the movement of the balls. The milling balls then crush the re-actants, as a result also providing the reaction energy by impact and friction. The perovskite powders synthesized using this method are often highly stable. (1,2)

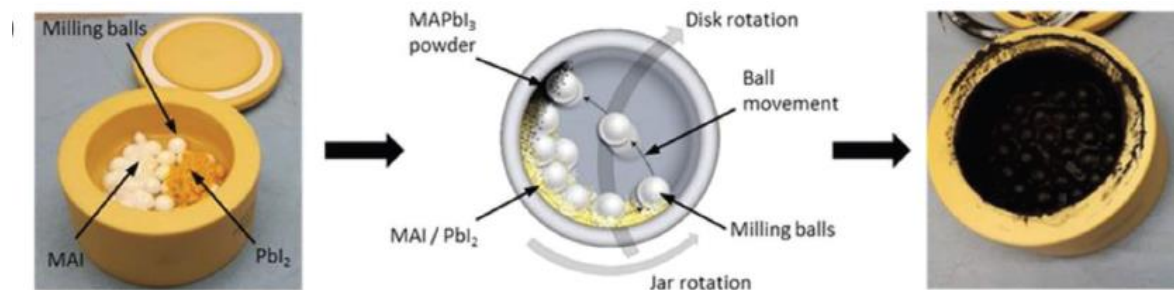


Figure 9 Schematic diagram of Mechanochemical synthesis (1)

3.2 Thermal Annealing

Thermal annealing is a solvent free method to produce halide perovskite powders. In this method the precursor powders (AX , BX_2) are first mixed in a chemical resistant reaction container such as quartz ampoules and sealed after mixing in order to avoid evaporation of components. The container is heated for several hours to 200 to 600 °C which then induces the diffusion of the reactants into each other resulting in the formation of perovskite. For this process, the high mobility of the ions in the perovskite lattice is beneficial. Due to the increased temperatures, sintering processes often occur, which on the one hand increase the crystal size, but on the other hand can also have the consequence that the individual powder particles sinter together too much, so that additional milling is needed before further processing. Due to the low decomposition temperature of hybrid perovskites that involve organic constituents (e.g., $MAPbI_3 \approx 240$ °C), the thermal annealing approach appears to be particularly suitable for inorganic perovskites such as $CsPbX_3$, which in general exhibit an increased decomposition temperature (e.g., $CsPbBr_3 \approx 560$ °C). However, mixed hybrid perovskites could be synthesized via thermal annealing when already synthesized ternary halide perovskites were used as precursors. (2)

3.3 Hot Injection

In this method one of the precursors is rapidly injected into a hot solution containing the remaining precursors, organic ligands and a high boiling solvent. This method is performed under an inert atmosphere. (4)

Oleic acid, Oleylamine and 1-octadecene are introduced into a three-neck flask and degassed for one hour under vacuum (10^{-2} mbar or better) at 80-100 °C. CsCO₃ is added and degassed for one hour at the same pressure and temperature. The flask is then flushed with N₂ and heated to 100 °C for one hour or until the CsCO₃ is completely dissolved. (3)

Simultaneously, the reaction mixture is heated according to the desired reaction temperature (typically 170 °C) before a solution of SnX₂ or PbX₂ (X=Cl,Br,I) and tri-n-octylphosphine is injected into the prepared Cs-precursor. (3)

The reaction vessel is then kept at the injection temperature for 1 min and then an ice-cold water bath is placed under the three-neck flask which then quenches the nanocrystal growth. Purification of the prepared nanocrystal is done in an Argon-filled glovebox (O₂, H₂O<1ppm). (3,4)

Perovskites containing bromide or iodide as the only halide component need to be purified by flocculation to turbidity using an equal volume of 1-Butanol and then re-suspending in hexane. This process can be repeated twice for better morphology. (3)

For chloride-containing samples the adding 1-butanol results in dissolution of nanocrystals and causing SnX₂ salts to precipitate. In order to obtain these crystals the crude reaction solution needs to be centrifuged and then supernatant is discarded. The nanocrystals should then be re-suspended in hexane. This process can also be performed twice. (3)

The final nanocrystal solution must be centrifuged at 4k rpm for 2 mins and then filtered through a 200 nm PTFE filter to remove aggregated material. (3,4)

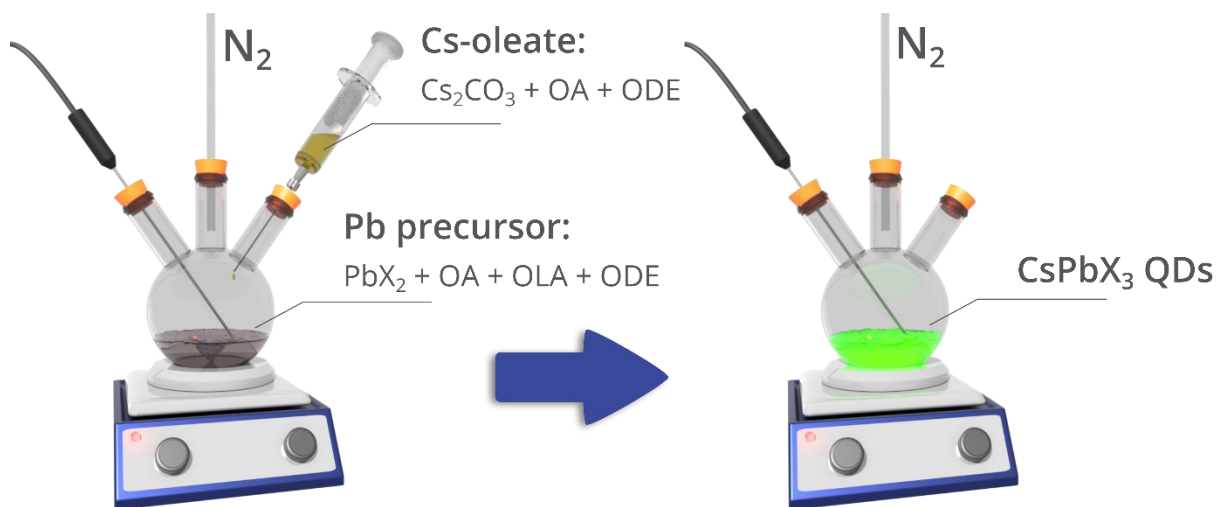


Figure 10 Schematic diagram of hot injection method (5)

3.4 Hydrothermal/Solvothermal method

The hydrothermal reaction is a heterogeneous chemical reaction that occurs in the presence of a solvent above atmospheric pressure and temperature. The principle of this method is that an insoluble material at temperature can be made soluble using high temperature and pressure. If water is used as solvent then the method is called hydrothermal and if any other solvent is used then this method is referred to as solvothermal. These reactions need to be performed in air-tight constant volume containers called hydrothermal autoclave reactors. In hydrothermal reactions, the reactors are heated at a fixed temperature above the boiling point of the solvent, and then the pressure builds up in the reactor by the vapor pressure of the solvent. In these conditions, solid phases crystallize from the reactants at the specific temperature and composition from the hydrothermal solution. So, any hydrothermal process can be distinguished as a combination of two steps: (i) the preparation of the precursor solution in a liquid phase, and (ii) the heating which determines the morphology. (6,7)

The generalized synthesis using a hydrothermal method is described as follows. The precursor salts are dissolved in a suitable solvent, sometimes an acid needs to be added, preferably at room temperature. To control the growth or morphology of the desired perovskites capping agents or surfactants may be added to the solution. Capping agents also play a role in stabilizing the nanostructured materials from agglomeration. Then, the reaction is carried in hydrothermal reaction vessels which is used to obtain the precursor for the perovskite. The final perovskite material is formed by calcinating the product from the reaction vessel for several hours at controlled heating. (6,7)

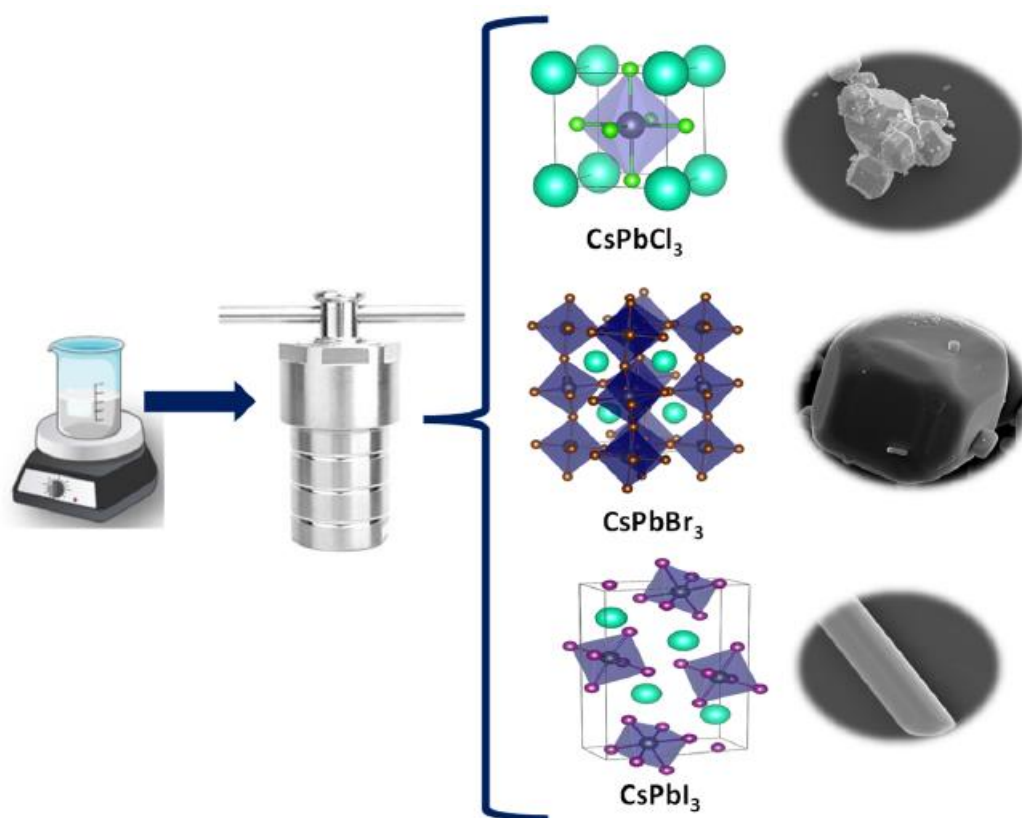


Figure 11 CsPbX₃ synthesis using hydrothermal method from precursor dispersion (6)

3.5 Sonochemical method

In this method the binary salts are dissolved in toluene, isopropanol, DMF, or glacial acetic acid. Using an ultrasonic bath, ultrasound is applied to the solution, which causes the crystallization of the perovskite. The ultrasound helps dissolve reactants and also plays a major role in forming the perovskite nuclei by collapsing acoustic bubbles of the precursor solution. Addition of organic ligands such as oleylamines to the synthesis process results in the production of perovskite nanocrystals. (1)

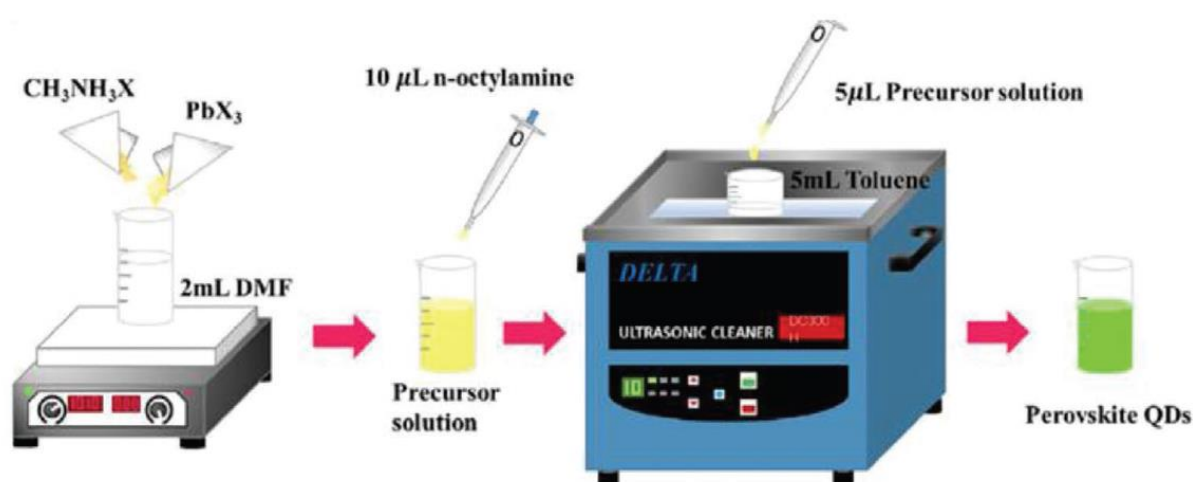


Figure 12 Schematic diagram of sonochemical method. (1)

3.6 Ligand assisted reprecipitation (LARP)

In this report, the $\text{CsPb}_{1-x}\text{Sn}_x\text{Cl}_3$ perovskite was synthesized using a modified LARP method. In general, the LARP method uses oleic acid and linoleic/oleylamine as ligands. DMSO is used as a solvent and Toulene, ethanol, chloroform or tetrahydrofuran (THF) are used as antisolvents.

In this method, the precursors are dissolved in Dimethyl Sulfoxide (DMSO) solvent to form the precursor solution which is stirred on a magnetic stirrer. Then the ligands are added to the

precursor solution. Ligands help control the formation of NCs. Then the antisolvent is added to the precursor solution containing ligands resulting in the formation of perovskite NCs.

In this method DMSO acts as a good polar solvent while Toluene, ethanol, hexane, etc. act as poor nonpolar solvents. The two solvents when mixed causes instantaneous supersaturation, which then induces the nucleation and the growth of perovskite NCs.

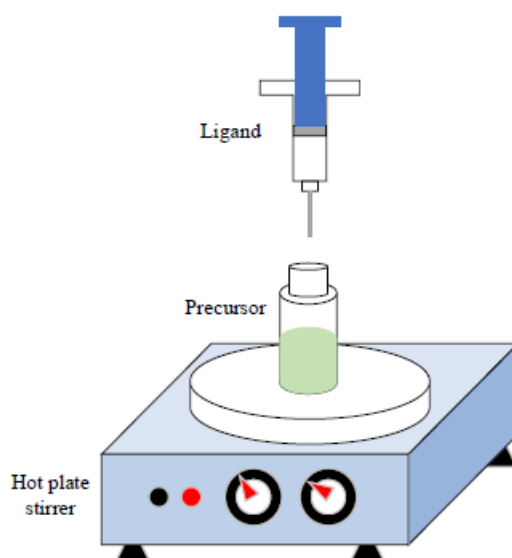


Figure 13 Schematic diagram for LARP synthesis method. (8)

3.6.1 Synthesis of $\text{CsPb}_{1-x}\text{Sn}_x\text{Cl}_3$

The chemicals used for the synthesis of $\text{CsPb}_{1-x}\text{Sn}_x\text{Cl}_3$ are PbCl_2 , CsCl , SnCl_2 , SnCl_4 , Toluene, Ethanol, DMSO and Oleic acid.

For 1.5 g of CsPbCl_3 0.5656 g CsCl , 0.9343 g PbCl_2 were weighed and added to a beaker followed by addition of 15 mL of DMSO. Then this beaker was placed on a magnetic stirrer and stirred for 30 mins, this results in the formation of precursor solution. (8, 9)

Simultaneously, 20 mL of toluene was kept in a ice bath and was stirred for 20 mins. After 30 mins of stirring, 1.5 mL of Oleic acid was added to the beaker containing the precursor solution and this solution is then stirred for another 15 mins followed by addition of the ice-bath cooled toluene. (8 9)

Addition of toluene results in precipitation and formation of perovskite NCs indicated by instantaneous colour change. The crude perovskite solution was then centrifuged for 30 mins at 1k rpm. After that, the supernatant was discarded and toluene was again added the centrifuging tubes and again centrifuged at 1k rpm for 10 mins. The resulting perovskite precipitate was then put on a petri dish and then was kept in a oven for drying. The perovskite NCs were dried at 90°C for 30-60 mins and the perovskite powder was formed.

For the Sn-doped CsPbCl_3 and CsSnCl_3 samples the same procedure was followed except that ethanol was added in place of toluene. (8, 9)

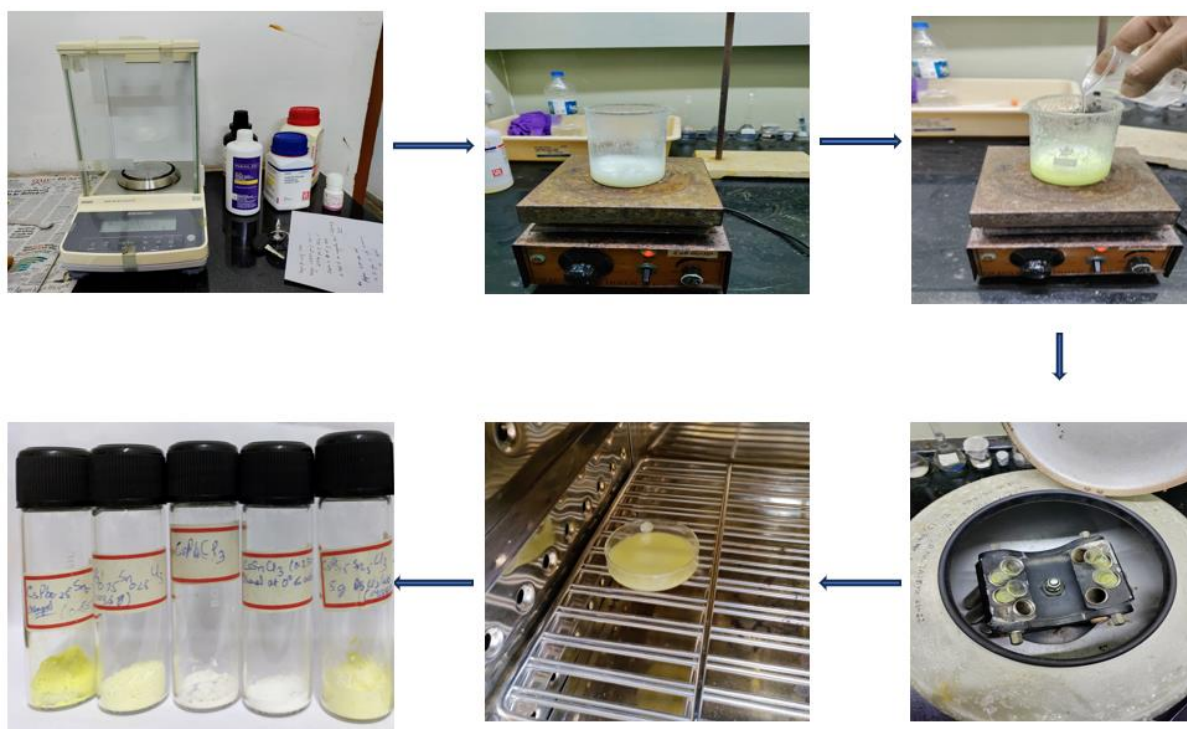


Figure 14 Steps involved in the synthesis of the $\text{CsPb}_{1-x}\text{Sn}_x\text{Cl}_3$ samples.

3.7 References

1. Leupold N, Panzer F. Recent Advances and Perspectives on Powder-Based Halide Perovskite Film Processing. *Advanced Functional Materials*. 2021 Apr;31(14):2007350.
2. Cheng J, Li Y, Qu W, Sun M, Liu Y, Shi W, Du W, Zhang Y. Mechanochemical synthesis and characterization of Mn-doped CsPbCl₃ perovskite nanocrystals. *Journal of Alloys and Compounds*. 2020 May 5;822:153615.
3. Jellicoe TC, Richter JM, Glass HF, Tabachnyk M, Brady R, Dutton SE, Rao A, Friend RH, Credgington D, Greenham NC, Böhm ML. Synthesis and optical properties of lead-free cesium tin halide perovskite nanocrystals. *Journal of the American Chemical Society*. 2016 Mar 9;138(9):2941-4.
4. Mu Y, He Z, Wang K, Pi X, Zhou S. Recent progress and future prospects on halide perovskite nanocrystals for optoelectronics and beyond. *Iscience*. 2022 Nov 18;25(11).
5. Fallows T. Oscilla.com. [Online].; 2019. Available from: <https://www.ossila.com/blogs/articles/perovskite-quantum-dot-synthesis>.
6. Echeverría-Arrondo C, Alvarez AO, Masi S, Fabregat-Santiago F, Porta FA. Electronic, Structural, Optical, and Electrical Properties of CsPbX₃ Powders (X= Cl, Br, and I) Prepared Using a Surfactant-Free Hydrothermal Approach. *Nanomanufacturing*. 2023 May 19;3(2):217-27.
7. Gibin George, Sivasankara Rao E, Zhiping L. Synthesis of Perovskite Oxides. In *Fundamentals of Perovskite Oxides Synthesis, Structure, Properties and Applications*.; 2020. p. 25-26.
8. Yandri VR, Wulandari P, Hidayat R. Photoluminescence Properties of CsPbCl₃ and CsPbBr₃ Nanocrystals synthesized by LARP Method with Various Ligands and Anti-

solvents. In *Journal of Physics: Conference Series* 2022 Jun 1 (Vol. 2243, No. 1, p. 012120). IOP Publishing.

9. Shamsi J, Urban AS, Imran M, De Trizio L, Manna L. Metal halide perovskite nanocrystals: synthesis, post-synthesis modifications, and their optical properties. *Chemical reviews*. 2019 Feb 13;119(5):3296-348.

4. CHARACTERIZATION TECHNIQUES

4.1 X-ray diffraction (XRD)

X-ray diffraction is a characterization technique which is non-destructive enabling it to be used for studying the microstructural properties of a material based on X-ray diffraction to determine the crystalline or amorphous nature of the material. (1)

X-ray diffraction has now become a common technique for studying crystal structures and atomic spacing. The basic principle of XRD is constructive interference of monochromatic X-rays and a crystalline sample. The X-rays are generated using a cathode ray tube, which are filtered to produce monochromatic radiation, which is then collimated to concentrate, and is directed toward onto the sample. Constructive interference will happen when the interaction between the incident ray and the sample satisfies Bragg's Law given as:

$$n\lambda = 2d \sin\theta$$

n is integer

λ is the wavelength of the incident X-rays

d is the interplanar spacing

θ is the diffraction angle.

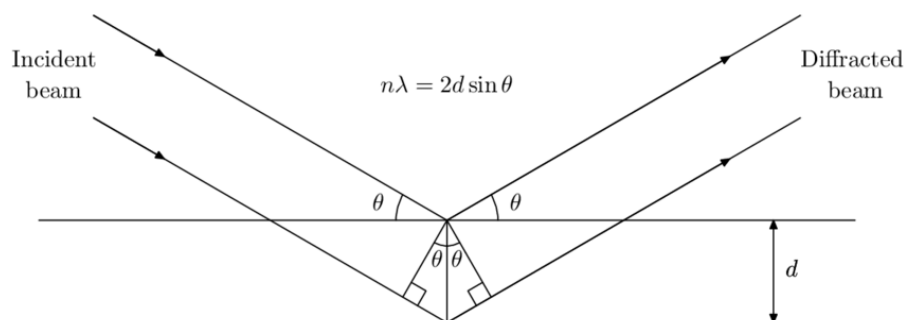


Figure 15 schematic diagram of Bragg's Law, (3)

The diffracted X-rays are then detected, processed and counted. Since, orientation of the powdered material is random, all the possible all possible diffraction directions of the lattice

must be attained, this is done by scanning the sample through a range of 2θ angles. Each compound has a set of unique d-spacings, thus by converting the diffraction peaks to d-spacing, the compound and its structure can be identified. Typically, this can be achieved by comparing d-spacings with standard reference patterns. (2)

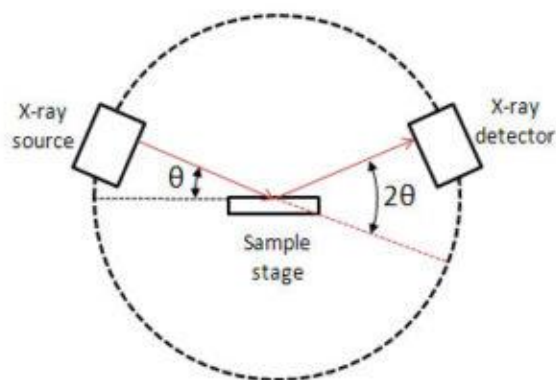


Figure 16 Schematic diagram of components of XRD diffractometer. (4)

The crystalline size can be calculated by using the Scherrer's formula given as:

$$D = \frac{0.9\lambda}{B\cos\theta}$$

In the above equation λ is the X-ray wavelength and B is the full width at half minimum (FWHM) of the diffraction peak and θ is the Bragg's angle. (1) In this dissertation, Rigaku MiniFlex diffractometer was used with a incident CuK_{α} radiation of 1.54 \AA .



Figure 17 Diffractometer used in the dissertation

4.2 UV-Visible Spectroscopy

It is analysis technique that compares ultraviolet and visible light that is absorbed or transmitted through a sample and reference sample using Beer-Lambert law. When a light of a certain specific wavelength hits a electron of the molecule it gets excited from the ground to a higher energy state. The electron with lower energy jumps to the higher energy state by absorbing light energy. (5)

Initially, light from the source is focussed on the monochromator. Monochromator separates the light by wavelength using optical grating. The light is passed into a charged coupled device (CCD) (consisting of individual tiny detectors) which measured the intensity of light at each wavelength. The CCD is read-off to the computer and the resulting spectrum is obtained, showing the intensity of each wavelength of light. (6)

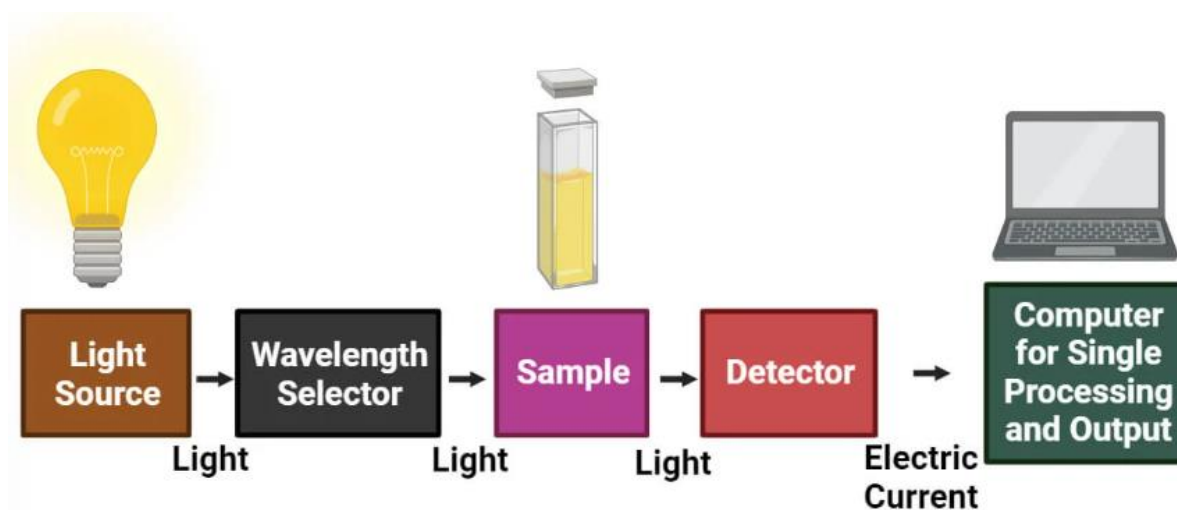


Figure 18 Schematic diagram of Uv-Vis spectrometer. (5)

Beer-Lambert law states that the absorbance is directly proportional to the concentration of the substance in the solution.

The Beer-Lambert Law is expressed in the following equation:

$$A = -\log T = -\log \frac{I}{I_0} = \log \frac{I_0}{I} = \epsilon cl$$

Where, A is the absorbance l is optical path length of cuvette (cm), c is concentration of the solution (M) and ϵ is the molar absorption coefficient ($M^{-1} \text{ cm}^{-1}$). This technique also allows the calculation of the optical bandgap using the Tauc relation equation which is given as:

$$\alpha hv = B(hv - E_g)^n$$

In the above equation α is the absorption coefficient (cm^{-1}), hv is the energy of the incident photon (eV), and B is the proportionality constant. n can have values 1/2 and 2 for direct and indirect bandgap respectively. The bandgap values are calculated from the plot of $(\alpha hv)^{1/n}$ vs. hv . (1,4)

4.3 Photoluminescence (PL) Spectroscopy

Photoluminescence spectroscopy is a method in which the electronic structure of the material is probed in a contactless and non-destructive manner. In this technique, light is used to strike the sample, where it gets absorbed and the excess energy is given to the material in a process called photo-excitation. This excess energy is then given out by the sample through the emission of light, or luminescence. This luminescence due to photo-excitation is called photoluminescence. (7)

Electrons get excited and jump to this permissible excited states due to photo-excitation. When these electrons come back to their equilibrium states they release the excess energy either by a radiative process or a nonradiative process. The radiative process leads to emission of light. The energy of the emitted light (photoluminescence) is equivalent to the

difference in energy levels between the excited state and the equilibrium state. The amount of the light emitted is related to the relative contribution of the radiative process.(7,8)

All solids, including semiconductors, have a energy gap for the conduction electrons. To understand the concept of a *energy gap*, we consider that some of the electrons in the solid are not bound to the atoms firmly, since they are for single atoms, but they can jump from one atom to another. Since these electrons are bound loosely in the solid by differing amounts which leads to them having much different energy. Those electrons which have energies above a certain value are called as conduction electrons which are found in the conduction band, and the electrons which have energies below a certain value are called as valence electrons which are placed in the valence band. Furthermore, there is an energy gap between the conduction and valence band as a result under normal conditions the valence band electrons cannot go to the conduction band and vice-versa, because these electrons cannot have energies between the valence and conduction bands. (7)

The atom consists of a nucleus surrounded by electrons. Since, every element has a specific number of electrons, their orbital structure with the atomic nucleus is unique. The electrons are placed in the orbital in a ordered and a predictable way. The ground state is the most stable electronic configuration of an atom as it has the lowest energy as a result it is the normal orbital configuration for an atom. (7)

When a certain specific amount of energy is given to an atom it will absorb the energy, as a result an outer electron will be transferred to the excited state which is less stable. Due to the instability of the excited state the atom will immediately and spontaneously return to its ground state by releasing radiant energy equivalent to energy that was absorbed during excitation process which will be emitted. (7,8)

Photoluminescence (PL) method can be used to characterize the electronic structure of the sample. During PL measurement, photons of the source light generate electron-hole pairs. The typical excitation energy for a photon is in the range of 0.3–6 eV, which is dependent on the bandgap of the material being investigated. The electrons and holes can recombine by radiative or non-radiative processes. Initially, electrons and holes are relaxed to the band edges by rapid non-radiative scattering processes. By measuring the photoluminescence spectrum we can extract valuable information from the band structure and the carrier states in quantum structures. (7)

A schematic diagram of the PL measurement setup is shown in figure 16. The sample is placed in a closed cycle helium cryostat wherein the temperature can be from 9 K to room temperature. An argon ion laser (wavelengths 488 nm, 514 nm) or a frequency doubled Nd:YVO laser (532 nm) is used for exciting the sample. The full width at half maximum of the intensity distribution of the laser beam focused on the sample surface is typically 100 μm .

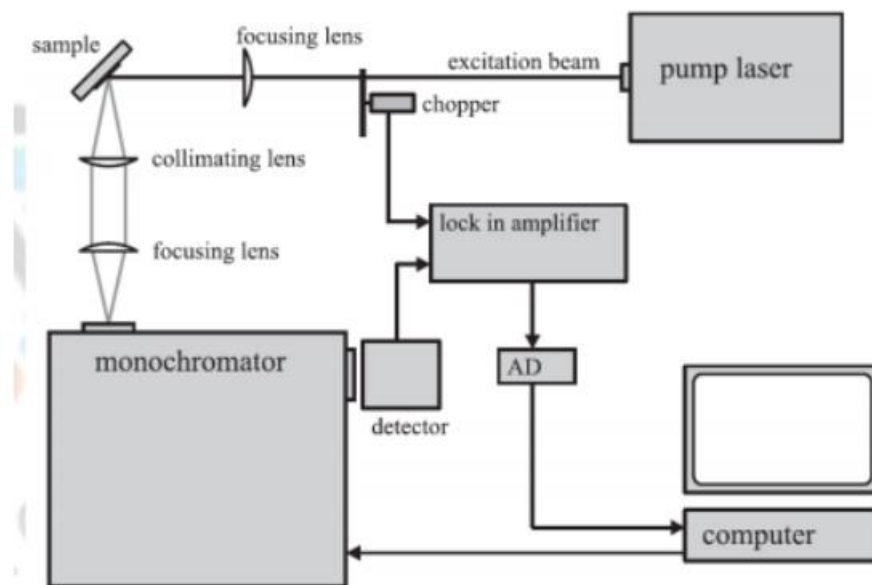


Figure 19 Schematic diagram of a photoluminescence setup. (7)

Two lenses are used to collect and focus the luminescence into a 0.5 m monochromator. The detector is liquid nitrogen cooled germanium pin-diode. The signal-noise ratio of the detection is improved by standard lock in technique. The monochromator is controlled and the measurement data is collected in a computer with an AD converter. (7)

4.4 Raman Spectroscopy

Raman Spectroscopy is a type of a non-destructive chemical analysis technique which can provide a detailed information regarding the chemical structure, phase, as well as, polymorphy, crystallinity and molecular interactions. It is basic principle of this spectroscopy is the interaction of light with the chemical bonds within a material. (9)

Raman spectroscopy is a light scattering technique in which the incident light from a high intensity laser light source is scattered by the molecule of the sample. When the light is incident on the molecule two types of scattering can take place, one wherein the light is scattered at the same wavelength as the incident laser light, this is called Rayleigh scattering and another type where in a small amount (0.0000001%) of light is scattered at a different wavelength which is depended on the chemical structure of the analyte. This type of scattering is known called Raman Scattering. (9,10)

A Raman spectrum features a number of peaks, showing the intensity and wavelength position of the Raman scattered light. Each peak corresponds to a specific molecular bond vibration, including individual bonds such as C-C, C=C, N-O, C-H etc., and groups of bonds such as benzene ring breathing mode, polymer chain vibrations, lattice modes, etc. (9)

Raman spectroscopy causes the interaction with the chemical structure of a material and provides information about chemical structure and identity, phase and polymorphism, intrinsic stress/strain as well as the contamination and impurity. (9)

Raman spectrum is a like unique chemical fingerprint for a particular molecule or material as a result can be used to quickly identify the material. (9) A typical Raman spectroscopy setup is shown in Figure 20.

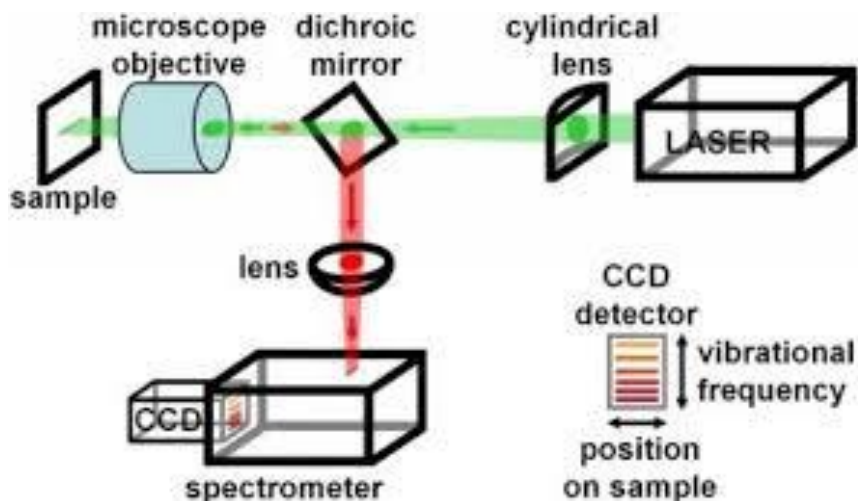


Figure 20 schematic diagram of Raman spectroscopy instrument. (10)

4.5 Scanning Electron Microscopy (SEM)

The scanning electron microscope (SEM) 2D imaging technique which uses a focused beam of high-energy electrons to generate different types of signals at the surface of solid specimens. The signals that are given from electron-sample interactions give information about the sample morphology (texture), and crystalline structure and orientation of materials in the sample. (11)

In this method, the data is collected from a selected area of the surface of the sample, and a 2D image displaying spatial variations in these properties is formed. SEM can scan an area of a sample with a ranging from 5 microns to 1 cm (magnification range is from 20X to 30,000X and spatial resolution of 50 to 100 nm). The SEM can also analyse a selected point locations one the sample as a result SEM can also be used to determine the chemical

compositions of the sample (using EDX mode), and also crystal structure and orientations (using EBSD mode). (11)

Accelerated electron beam in SEM carries a large amount of kinetic energy, and this energy is dissipated in the form of different signals produced by electron-sample interactions as the incident electrons are decelerated in the solid sample. Different signals produced from electron sample interactions include secondary electrons (used for producing SEM images), backscattered electrons (BSE), Auger electrons, diffracted backscattered electrons, characteristic X-rays (for elemental analysis using EDX), sometimes even visible light (cathodoluminescence), and also heat. Images of samples are formed by detecting the secondary electrons and backscattered electrons. Morphology and topography of samples is seen by detecting the secondary electrons while, backscattered electrons detection illustrates the contrasts in composition in multiphase samples. Characteristic X-rays are generated due to the inelastic collisions of the incident electrons with inner shell electrons of atoms in the sample. As the excited electrons return back to their lower energy states by emitting X-rays that are of a fixed wavelength. Thus, characteristic X-rays are unique to each element which gives the elemental composition of sample. SEM is considered as non-destructive technique which means that the same sample can be imaged or analysed repeatedly since, generated X-rays do not lead to a loss in volume of the sample.(11)

Essential components of all SEMs include the Electron Source Gun, Electromagnetic Lenses, Sample Stage, Detectors, Display and Data output devices

Infrastructural requirements for SEM include a high-power Supply, vacuum System and cooling system, a Vibration-free floor and Room free of ambient magnetic and electric fields. SEMs usually are mostly used for imaging so a secondary electron detector is always there and the capabilities of the instrument are critically dependent on the detectors that it uses.(11)

In this method a high energy electron beam is generated by the electron gun (cathode) which requires a high voltage. The generated electron beam is then accelerated and focused by applying positive voltage to the anode and the generated electron beam is focused and given a direction onto the sample using the condenser and objective lenses and apertures and the scanning coils and the generated signal are detected using various detectors. This instrument needs a ultra high vacuum so that the electron beam does not interact with anything except the surface of the sample. (11)

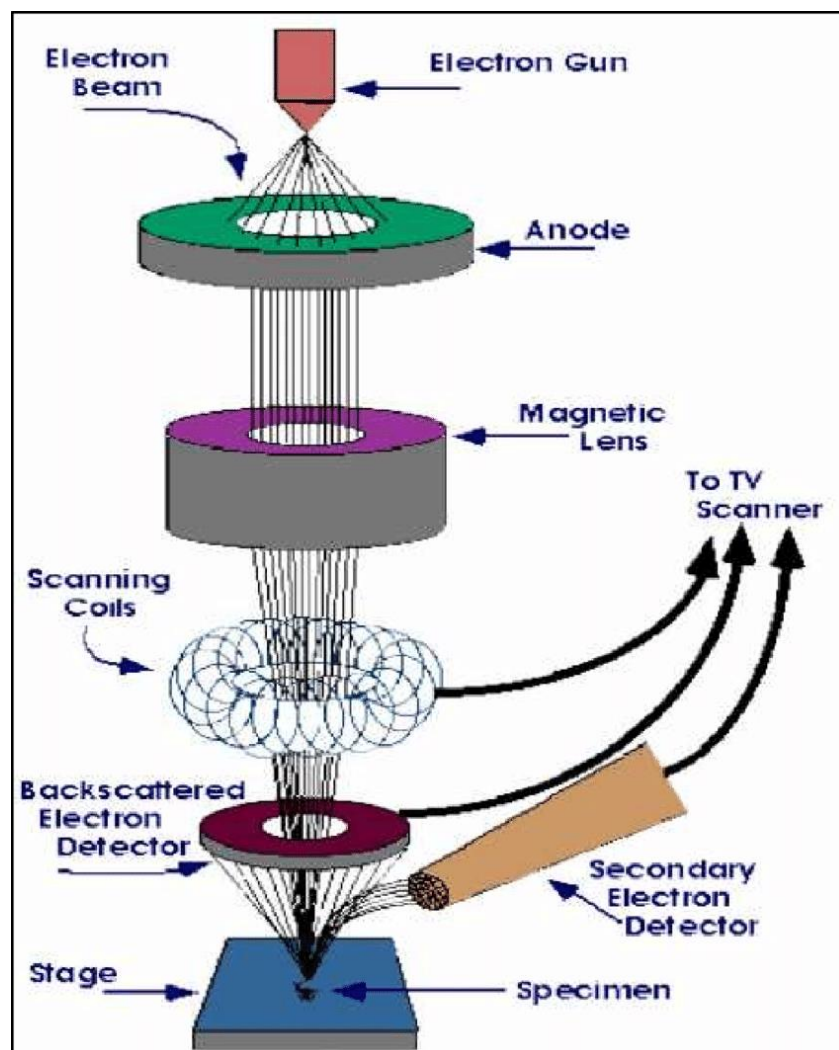


Figure 21 Schematic diagram of a scanning electron microscope. (12)

4.6 References

1. Basumatary P. Fabrication and studies of MAPbI₃ Perovskite Thin Films and Solar Cells. Thesis. Guwhati: Indian Institute of Technology, School of Energy Science and Engineering; 2022.
2. Bunaciu AA, Udriștioiu EG, Aboul-Enein HY. X-ray diffraction: instrumentation and applications. *Critical reviews in analytical chemistry*. 2015 Oct 2;45(4):289-99.
3. Sochi T. High throughput software for powder diffraction and its application to heterogeneous catalysis. arXiv preprint arXiv:1012.4506. 2010 Dec 20.
4. xrd.co. [Online]. [cited 2024]. Available from: <https://xrd.co/category/x-ray-diffractometer/>.
5. Shrestha P. Microbe Notes. [Online].; 2023. Available from: <https://microbenotes.com/uv-vis-spectroscopy/>.
6. SMACgigWORLD. [Online]. [cited 2024]. Available from: <https://www.smacgigworld.com/blog/design-and-working-uv-vis-spectrophotometer.php>.
7. Srivastava A. Nanoscience and Nanotechnology ii. [Online]. [cited 2024 April 28]. Available from: <https://ebooks.inflibnet.ac.in/msp09/chapter/photoluminescence-pl-spectra/>.
8. Christie MI. Photoluminescence. *Nature*. 1968; 220(5173): 1258-1258.
9. Horiba Scientific. [Online]. [cited 2024]. Available from: <https://www.horiba.com/int/scientific/technologies/raman-imaging-and-spectroscopy/raman->

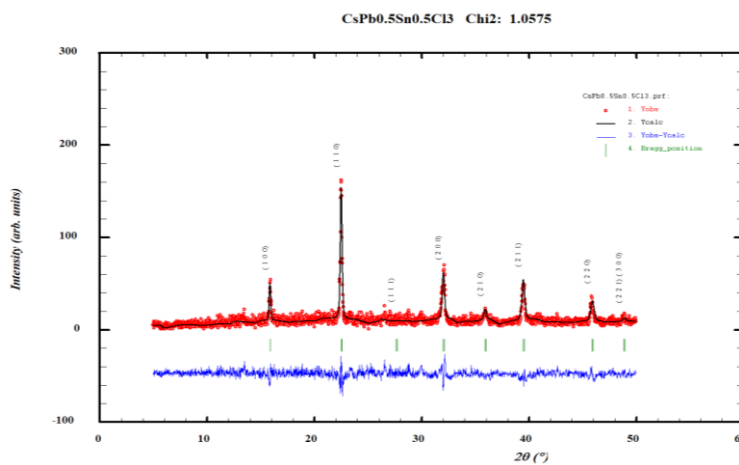
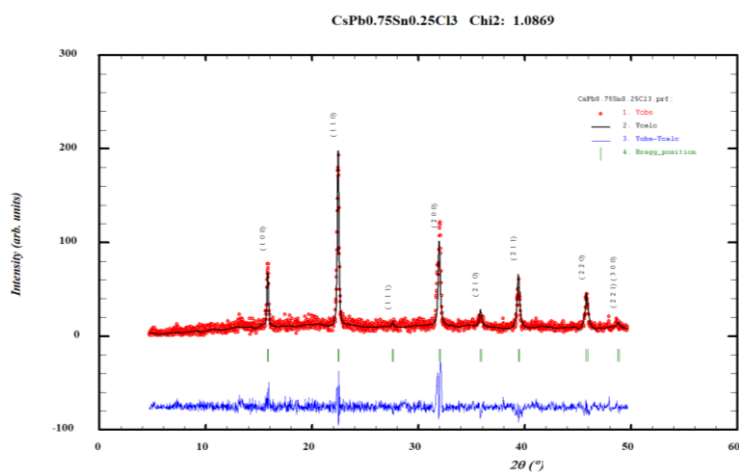
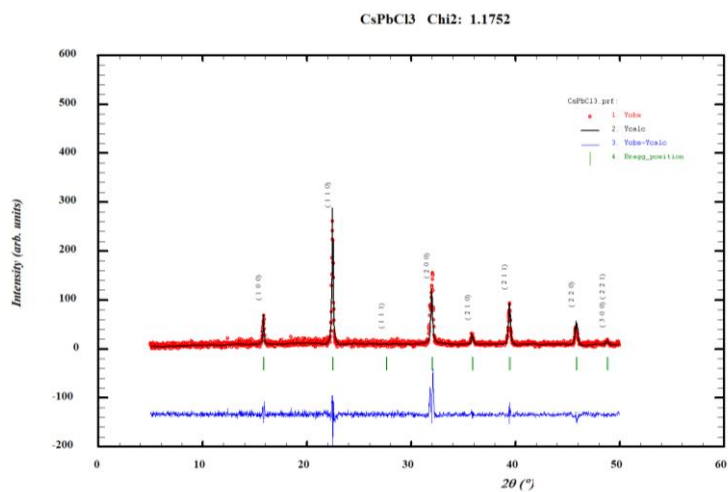
[spectroscopy/#:~:text=Raman%20Spectroscopy%20is%20a%20non,chemical%20bonds%20within%20a%20material.](#)

10. Downes A, Elfick A. Raman spectroscopy and related techniques in biomedicine. *Sensors*. 2010 Mar 9;10(3):1871-89.
11. Susan Swapp UoW. Science Education Resource Center at Carleton College. [Online]. [cited 2024. Available from: https://serc.carleton.edu/research_education/geochemsheets/techniques/SEM.html.
12. [Online]. Available from: <https://www.purdue.edu/ehps/rem/laboratory/equipment%20safety/Research%20Equipment/sem.html>.

5. RESULTS

5.1 X-ray Diffraction

The structural properties of the as-prepared samples were studied using powder X-ray diffraction technique using Rikagu MiniFlex diffractometer using Cu-K α radiation ($\lambda=1.54\text{\AA}$).



XRD analysis after Rietveld refinement revealed that all the samples had been crystallized in a cubic phase with $\text{CsPb}_{1-x}\text{Sn}_x\text{Cl}_3$ having $Pm\bar{3}m$ space-group and Cs_2SnCl_6 having $Fm\bar{3}m$ space-group. All $\text{CsPb}_{1-x}\text{Sn}_x\text{Cl}_3$ had near constant lattice parameters with CsPbCl_3 having $a=5.62391 \text{ \AA}$, $\text{CsPb}_{0.75}\text{Sn}_{0.25}\text{Cl}_3$ having $a=5.61394 \text{ \AA}$, $\text{CsPb}_{0.5}\text{Sn}_{0.5}\text{Cl}_3$ having $a=5.6083 \text{ \AA}$ and $\text{CsPb}_{0.25}\text{Sn}_{0.75}\text{Cl}_3$ having $a=5.6055 \text{ \AA}$ while, Cs_2SnCl_6 had $a=10.4209 \text{ \AA}$. The Crystalline size and lattice strain of the prepared samples respectively are 36 nm and 0.004263 for CsPbCl_3 ; 32 nm and 0.004798 for $\text{CsPb}_{0.75}\text{Sn}_{0.25}\text{Cl}_3$; 35 nm and 0.004279 for $\text{CsPb}_{0.5}\text{Sn}_{0.5}\text{Cl}_3$; 41 nm and 0.004252 for $\text{CsPb}_{0.25}\text{Sn}_{0.75}\text{Cl}_3$; and 33 nm and 0.004127 for Cs_2SnCl_6 . (1, 2, 3, 9, 10, 11)

5.2 UV-Visible Spectroscopy

The optoelectronic properties were studied using UV-Vis spectroscopy in which the powder setup was used, with Barium Sulphide as the baseline. The setup and the slot for for putting the powder is shown in the figure 23.



Figure 23 UV-Vis spectroscopy setup for powder sample

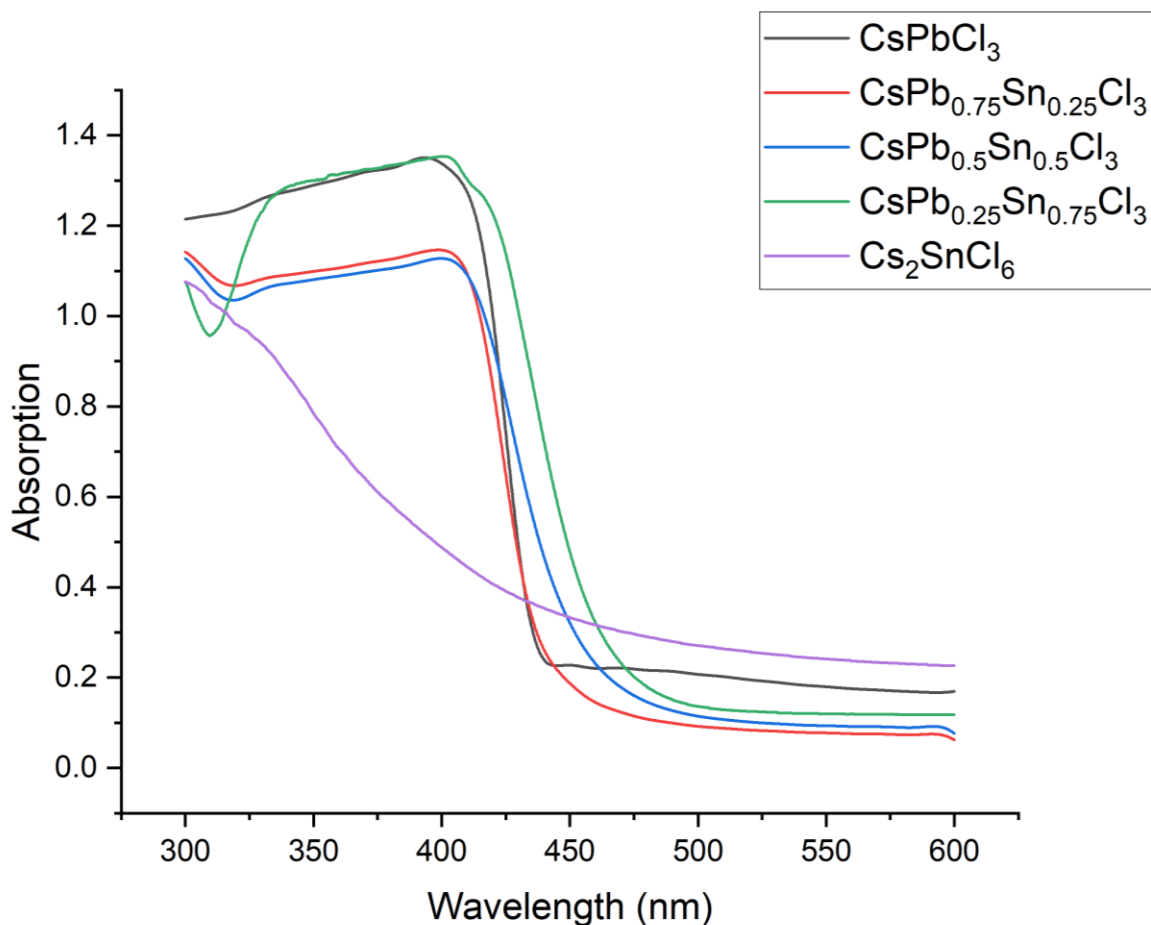
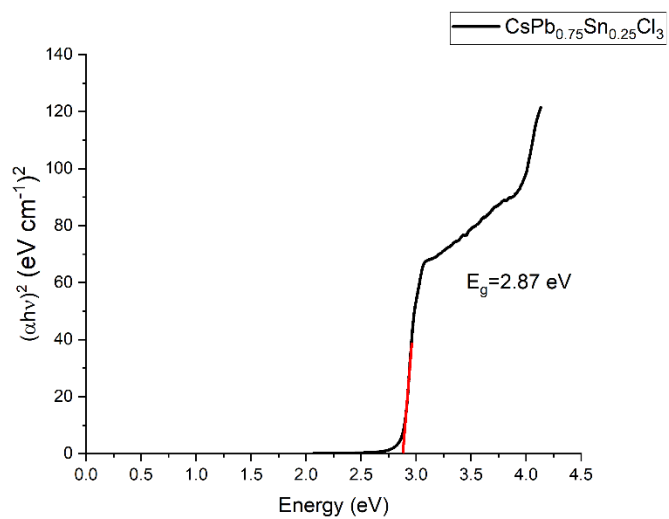
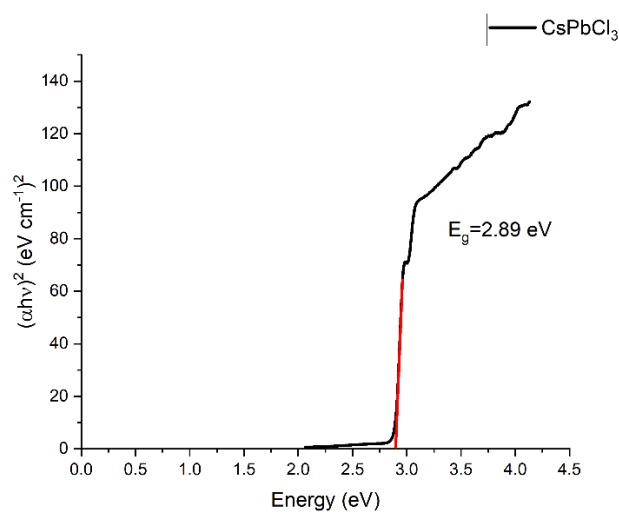


Figure 24 Absorption spectra of $\text{CsPb}_{1-x}\text{Sn}_x\text{Cl}_3$ ($X = 0, 0.25, 0.5, 0.75$) and Cs_2SnCl_6

From the Absorption v/s wavelength plot, the absorption peak for undoped CsPbCl_3 is observed at 394 nm which is in good agreement with the previous results from the literature.

(1) For the doped samples as the doping increases from 0.25-0.75 the peaks are observed at 399 nm, 401 nm, and 403 nm. There is a slight redshift as move from the doping ratio of 0.25 to 0.75 indicating that Sn has been doped into the host CsPbCl_3 . This observed redshift maybe because Sn^{2+} doping leads to lattice contraction which increases the halide orbital overlap of halide p -orbital and metal s -orbital which raises the band (valence band maximum) to shallower energies. Also the $[\text{SnCl}_6]$ octahedra contracts as compared to $[\text{PbCl}_6]$ octahedra which tilts (which increases the metal halide orbital overlap) as a result of the contraction band energies become shallower, along with this Sn $5s$ lone pair is more shallower and active

than Pb $6s$ lone pair. All these factors result in the redshift along with the reduction in bandgap (this can be seen from Figure 24). (16, 17) Cs_2SnCl_6 has been formed instead of CsSnCl_3 indicated by the Absorption spectra. The absorption peak could not be found as it was beyond the range of the instrument.



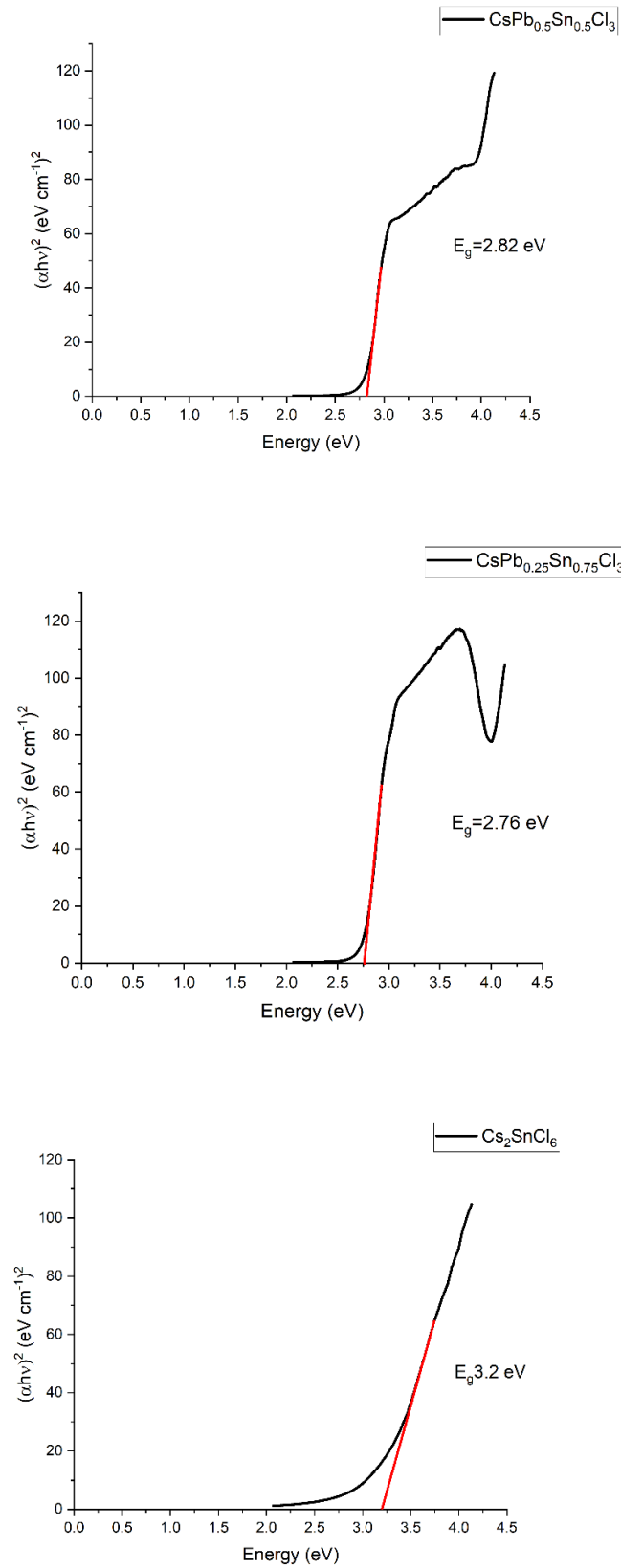
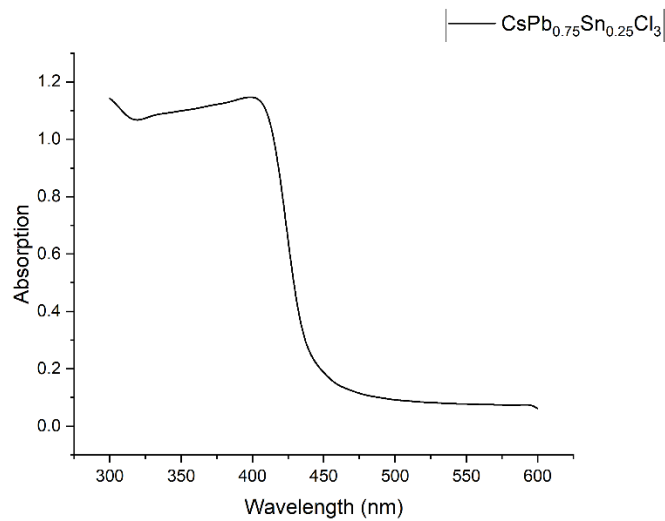
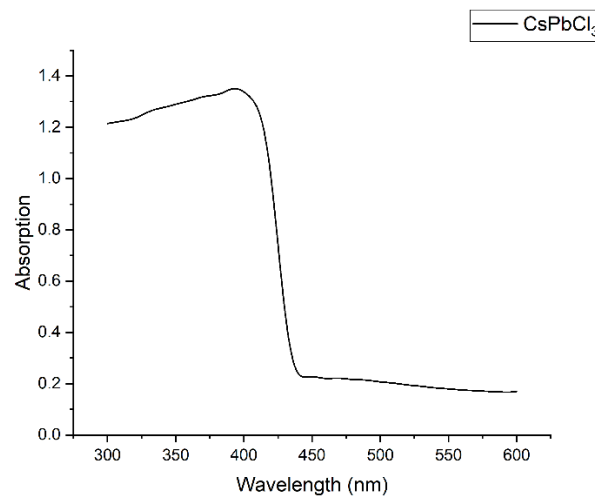


Figure 25 Tauc plots of $(\alpha h\nu)^2$ v/s energy for $\text{CsPb}_{1-x}\text{Sn}_x\text{Cl}_3$ and Cs_2SnCl_6

All the as-prepared samples have a direct bandgap. The bandgaps for $\text{CsPb}_{1-x}\text{Sn}_x\text{Cl}_3$ for x between 0 to 0.75 are found to be 2.89 eV, 2.87 eV, 2.82 eV, and 2.76 eV respectively. The bandgaps are found to decrease as we increase the Sn doping concentration which is good for solar cell applications. Bandgap for Cs_2SnCl_6 was found to be 3.2 eV. (1,9)



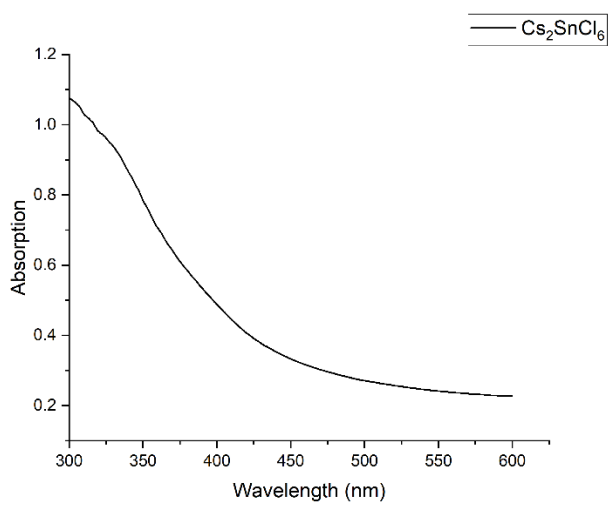
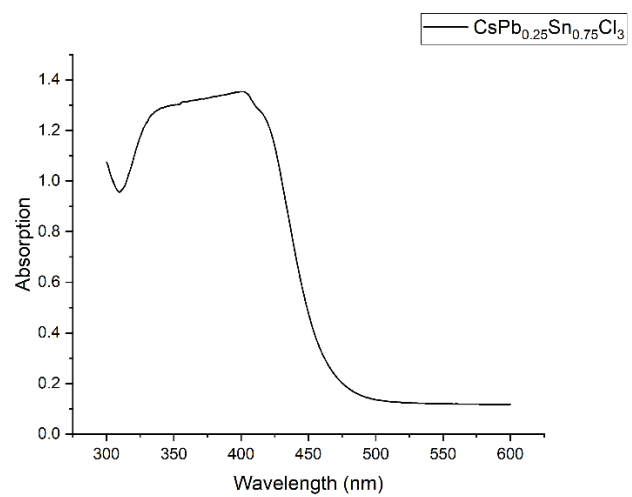
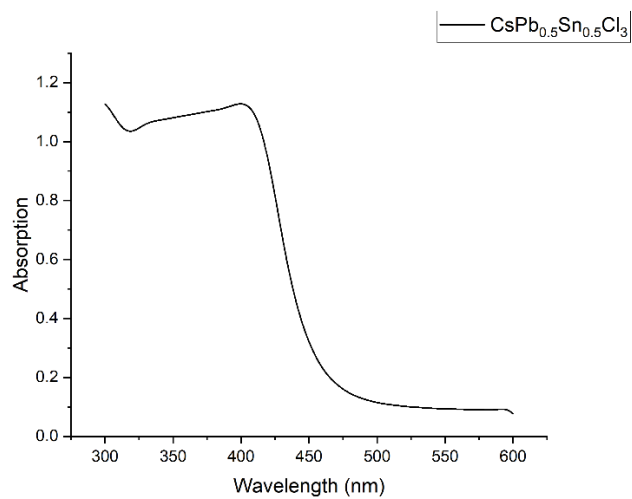


Figure 26 Absorption spectras for $\text{CsPb}_{1-x}\text{Sn}_x\text{Cl}_3$ ($x=0, 0.25, 0.5, 0.75$) and Cs_2SnCl_6 .

5.3 Photoluminescence spectroscopy

The emission spectra of $\text{CsPb}_x\text{Sn}_{1-x}\text{Cl}_3$ and Cs_2SnCl_6 were found using PL spectroscopy. The samples were dispersed using cyclohexane in a 1 cm cuvette. The samples were excited at a wavelength of 340 nm.

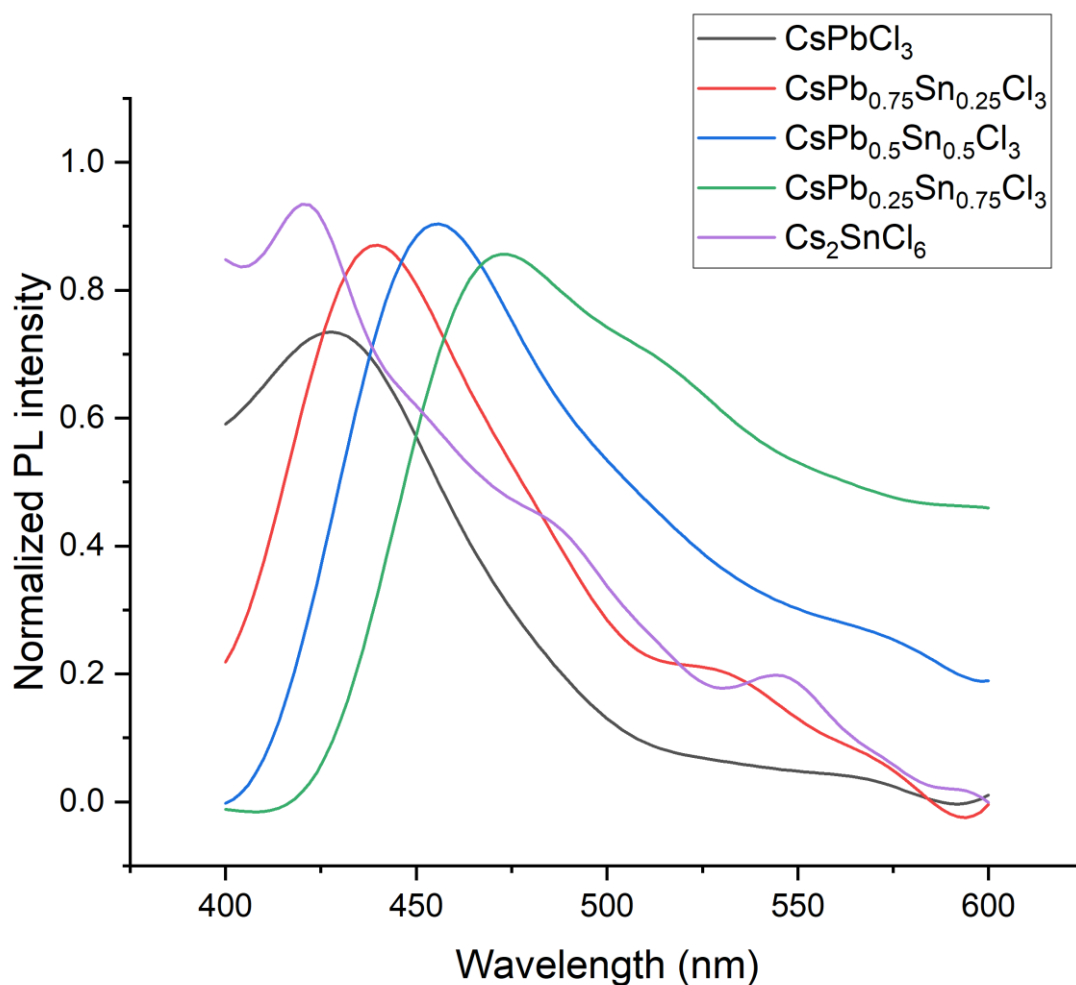
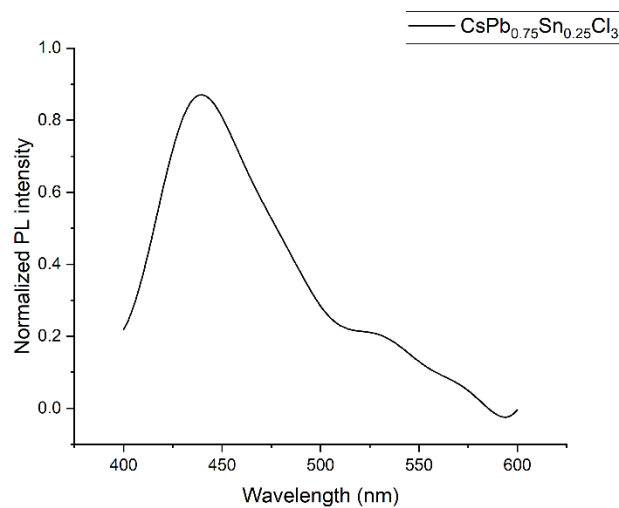
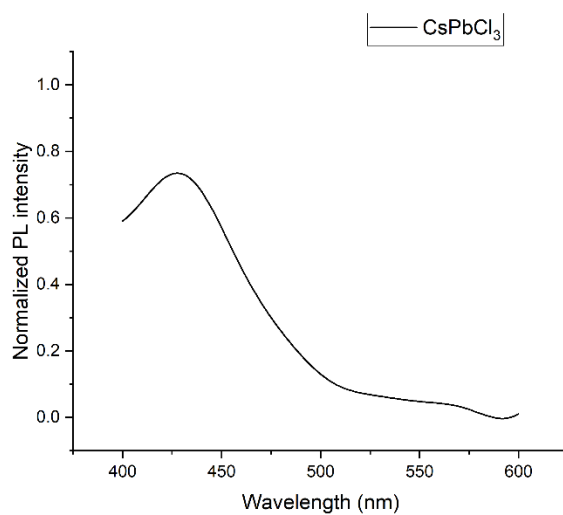


Figure 27 PL spectrum of $\text{CsPb}_{1-x}\text{Sn}_x\text{Cl}_3$ and Cs_2SnCl_6

The emission wavelength for undoped CsPbCl_3 is found to be 421 nm which is in agreement with the literature. Emission wavelength for $\text{CsPb}_{1-x}\text{Sn}_x\text{Cl}_3$ for X between 0.25 to 0.75 are 439 nm, 455 nm, and 473 nm respectively. We can see a good redshift as we move from X=0 to X=0.75, Sn doping shifts the emission to wavelength. Cs_2SnCl_6 has an emission peak at 420 nm. The PL spectra in CsPbCl_3 originates from the band tail, which can emerge from

disordered/defect states on the NC surface. Since the interaction between the Cl^- anion and Cs^+ and Pb^{2+} cations is strong, even stronger than those ion's interaction with the ligand as a result they rapidly form 3D $\text{CsPb}_{1-x}\text{Sn}_x\text{Cl}_3$ NCs during the anti-solvent dropping step. (1, 2, 3, 4)



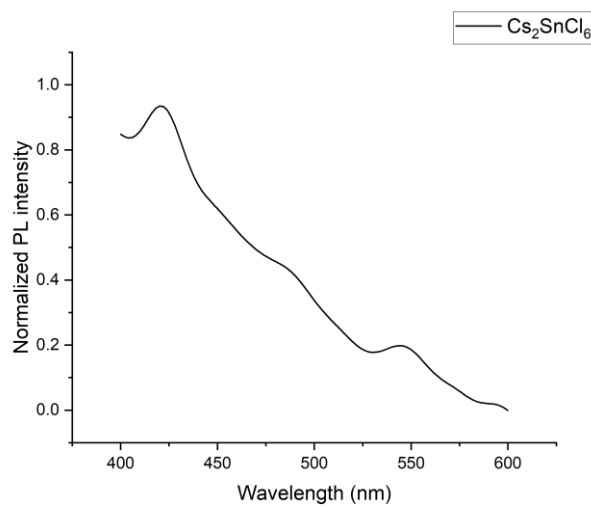
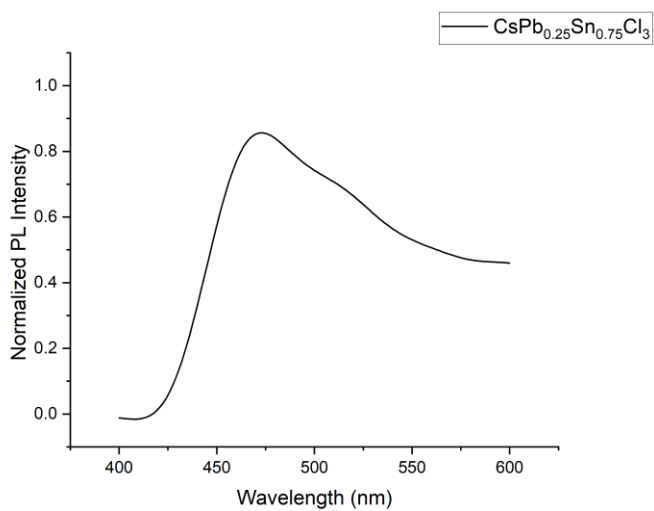
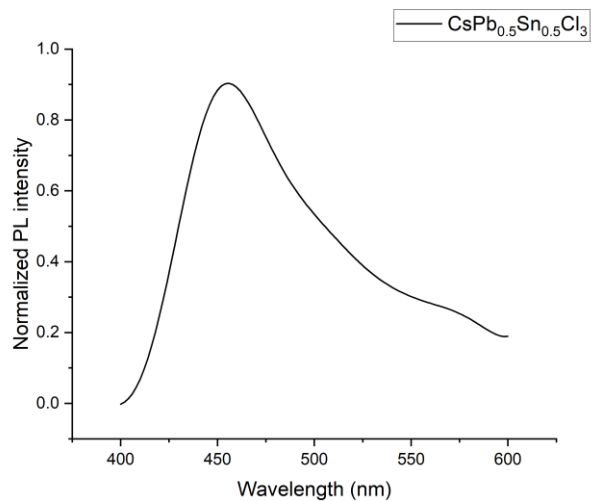


Figure 28 PL spectrum of $\text{CsPb}_{1-x}\text{Sn}_x\text{Cl}_3$ ($x=0, 0.25, 0.5, 0.75$) and Cs_2SnCl_6

5.4 Scanning electron microscopy

Carl Zeiss scanning electron microscope was used to study the morphology of the samples. The samples were sputter coated with a thin coating of a conductive material.

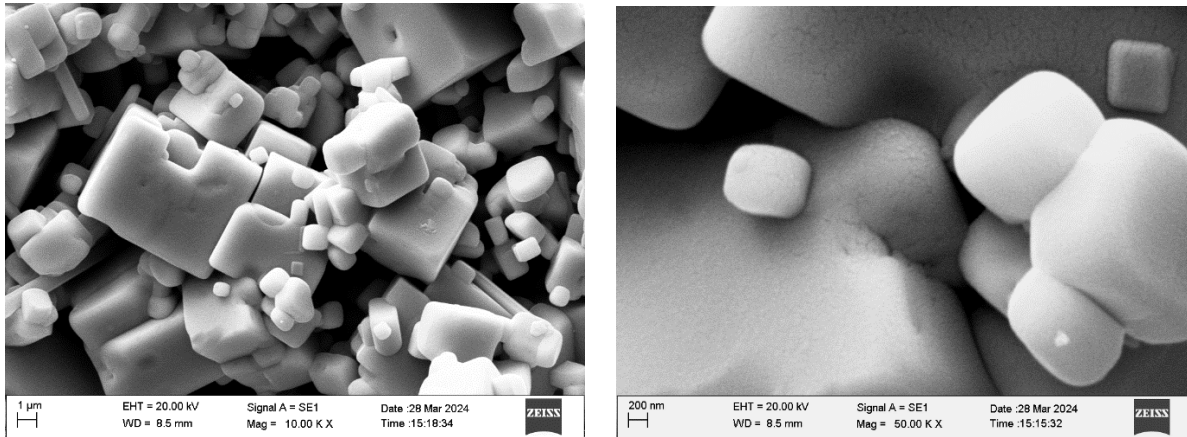


Figure 29 SEM images of CsPbCl_3 at $10\mu\text{m}$ and 200 nm

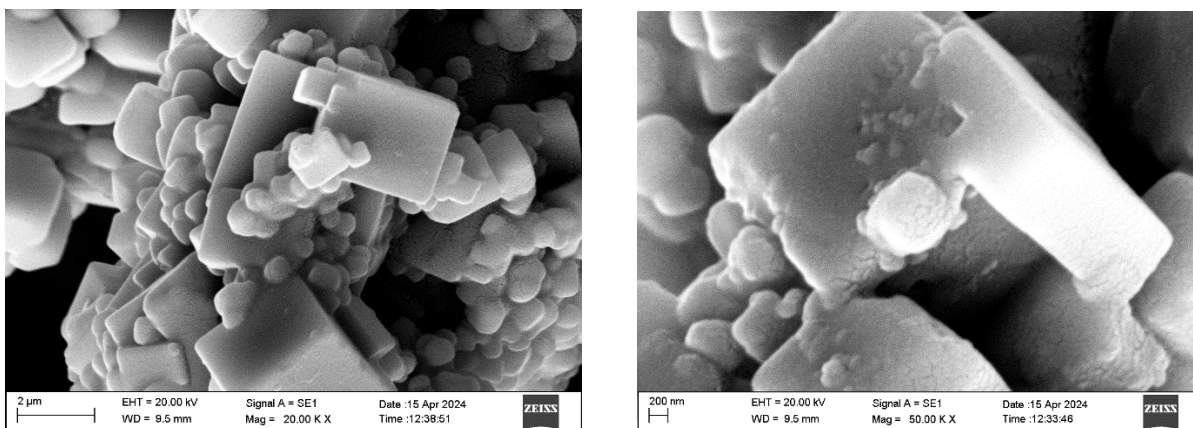


Figure 30 SEM images of $\text{CsPb}_{0.75}\text{Sn}_{0.25}\text{Cl}_3$

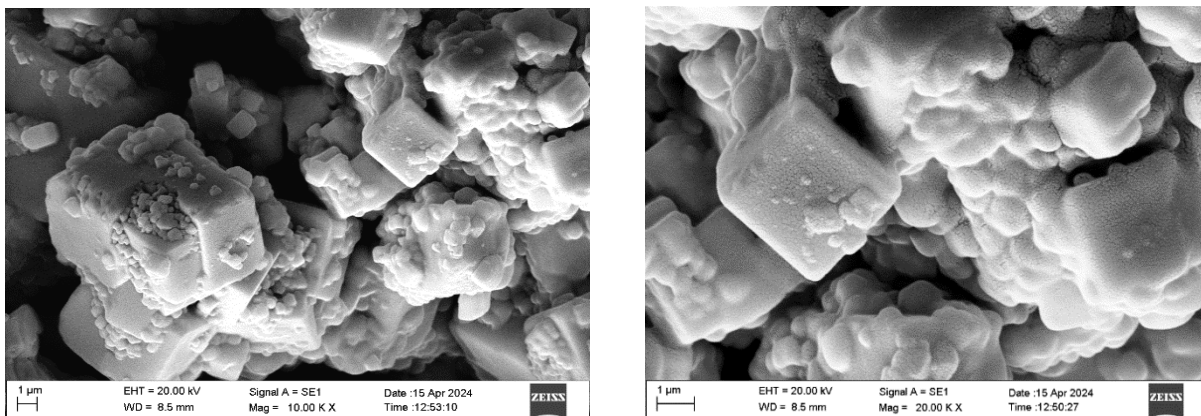


Figure 31 SEM images of $\text{CsPb}_{0.5}\text{Sn}_{0.5}\text{Cl}_3$

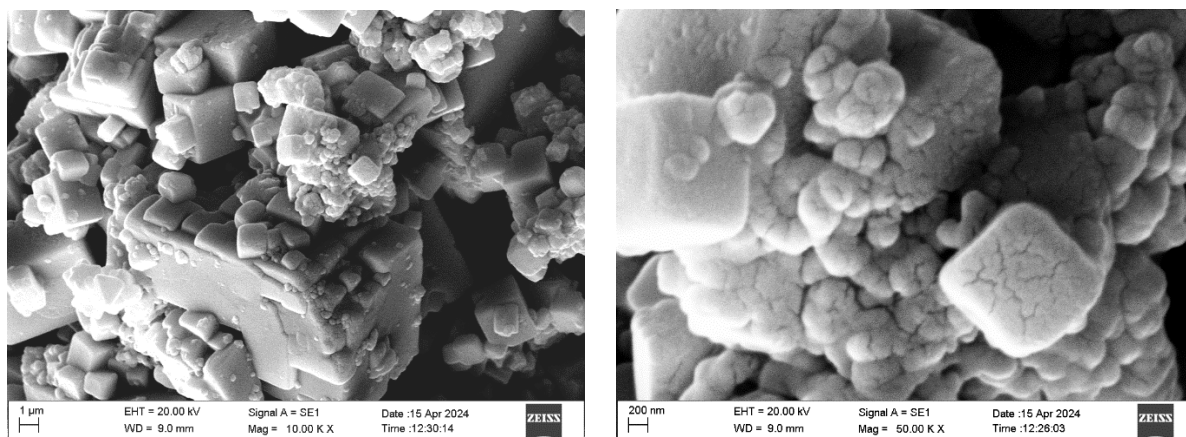


Figure 32 SEM images of $CsPb_{0.25}Sn_{0.75}Cl_3$

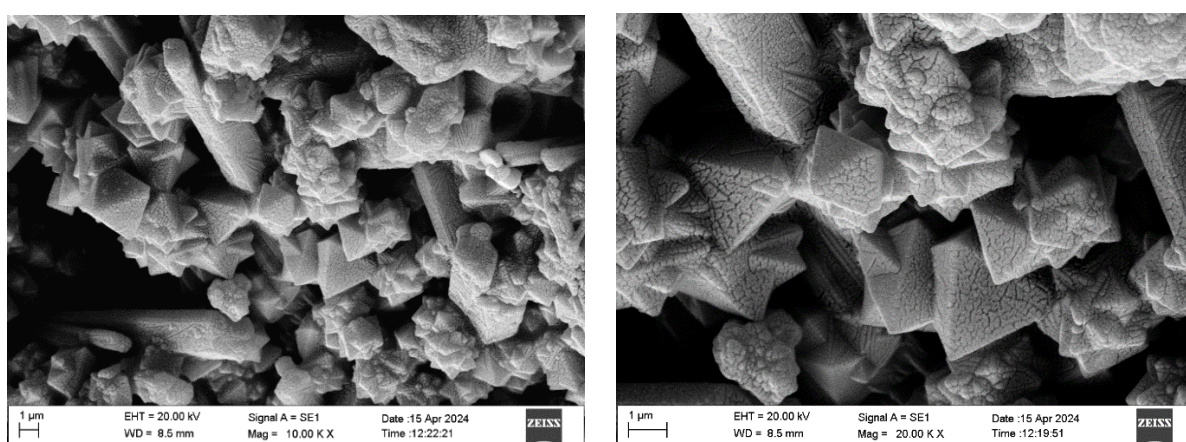


Figure 33 SEM images of Cs_2SnCl_6

The SEM revealed cubic morphologies of the as-prepared samples with a good crystalline size even in the nanometre range indicating the formations of nanocrystals. (5, 6 7, 8) Cs_2SnCl_6 was formed in a incomplete octahedron morphology as seen on Figure 27 with good growth and particle size. (9, 10, 11)

5.5 Raman spectroscopy

The chemical and vibrational studies of the prepared samples were done using Raman spectroscopy. LabRam HR Evolution Raman microscope was used to acquire the Raman spectra. The spectra was acquired by hitting the sample with a 532 nm laser.



Figure 34 Instrument used for acquiring raman spectra

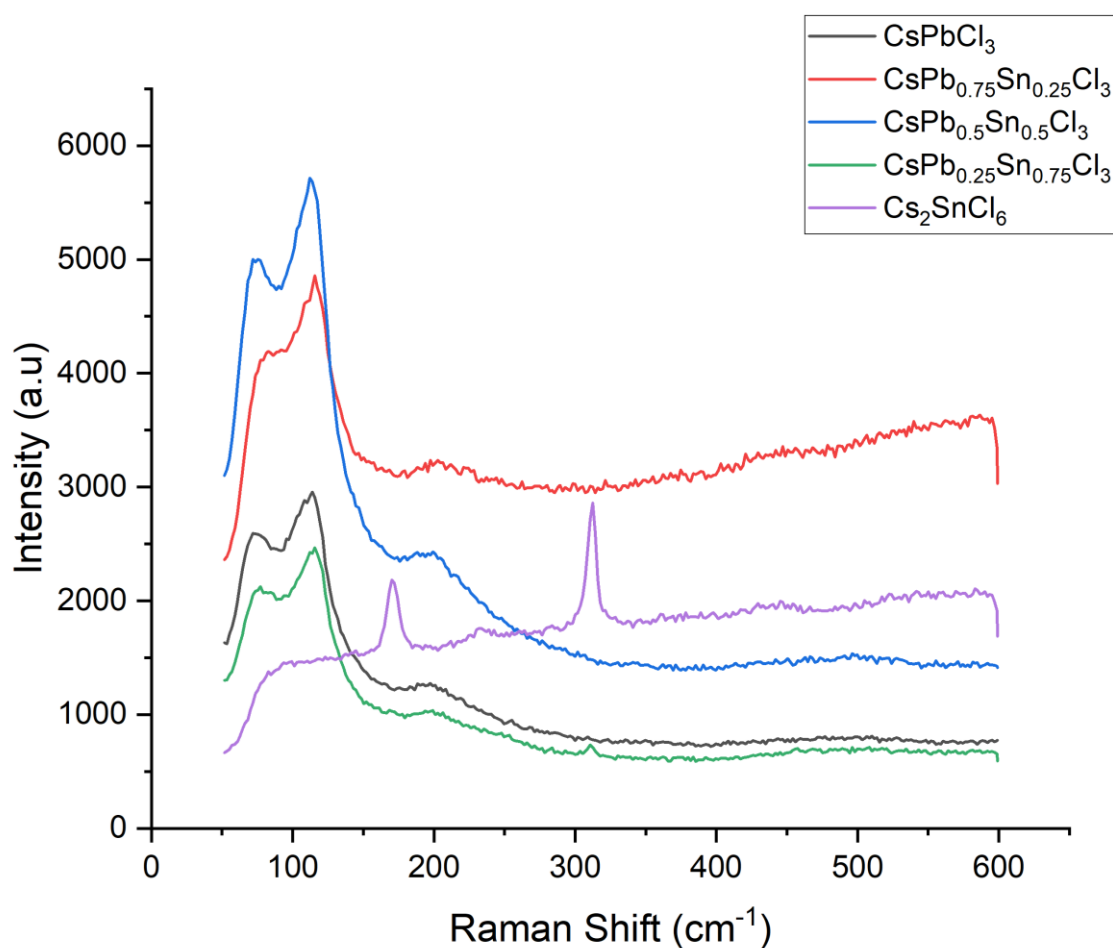
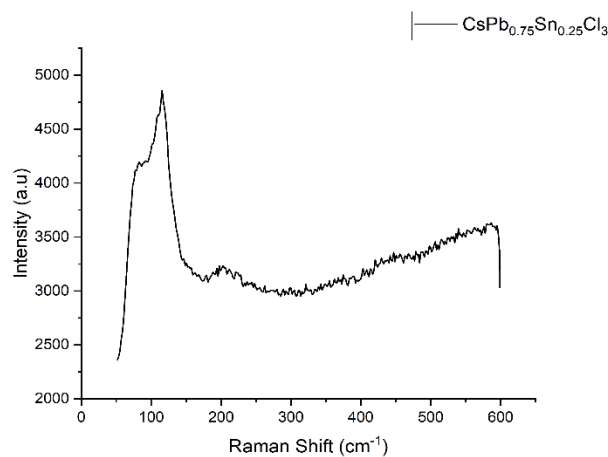
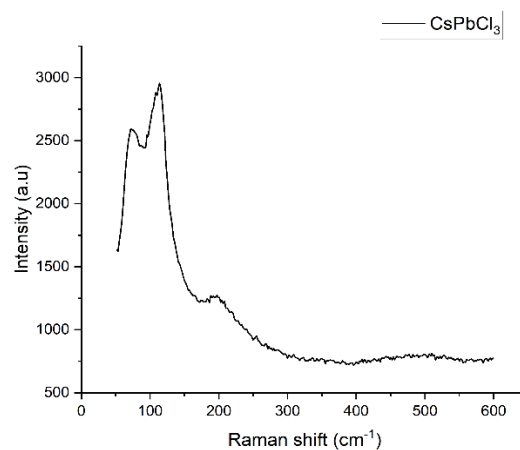


Figure 35 Raman spectra of prepared samples.

The obtained Raman spectra are shown in Figure 35. Three Raman active modes have been observed for the $\text{CsPb}_{1-x}\text{Sn}_x\text{Cl}_3$ as can be seen in the Figure 29. Undoped CsPbCl_3 possess

three non-degenerate longitudinal optical (LO) phonon modes and three doubly-degenerate transverse optical (TO) phonon modes. In this $\omega_{LO} > \omega_{TO}$ here, ω_{LO} and ω_{TO} are the frequencies of longitudinal and transverse phonon modes respectively. Three Raman active modes at $(68, 86) \text{ cm}^{-1}$, $(94, 121) \text{ cm}^{-1}$ and $(173, 220) \text{ cm}^{-1}$. The $(94, 121) \text{ cm}^{-1}$ is related to the $[\text{PbCl}_6]$ octahedron while the $(173, 22) \text{ cm}^{-1}$ is related to the motion of caesium atoms. In Cs_2PbCl_6 , three Raman active modes are related to vibrations in SnCl_6 octahedra which are $\nu(\text{A}_{1g})=312 \text{ cm}^{-1}$ due to the Sn-X symmetric stretching $\nu(\text{E}_g)=231 \text{ cm}^{-1}$ due to asymmetric stretching and $\delta(\text{F}_{2g})=170 \text{ cm}^{-1}$ for the X-Sn-X deformation. (8, 13, 14, 15)



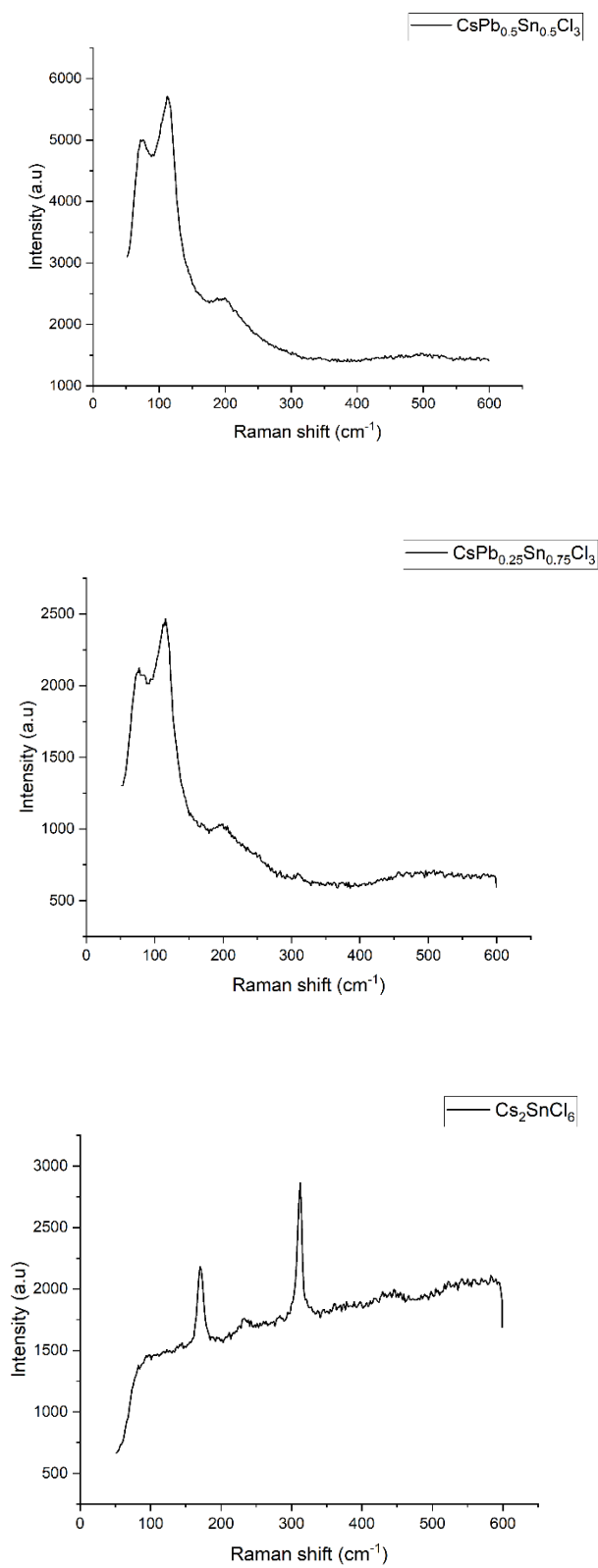


Figure 36 Raman spectras of CsPb_{1-x}Sn_xCl₃ ($x=0, 0.25, 0.5, 0.75$) and Cs₂SnCl₆

5.6 References

1. Pandey N, Kumar A, Chakrabarti S. Investigation of the structural, electronic, and optical properties of Mn-doped CsPbCl₃: theory and experiment. *RSC advances*. 2019;9(51):29556-65.
2. Jellicoe TC, Richter JM, Glass HF, Tabachnyk M, Brady R, Dutton SE, Rao A, Friend RH, Credgington D, Greenham NC, Böhm ML. Synthesis and optical properties of lead-free cesium tin halide perovskite nanocrystals. *Journal of the American Chemical Society*. 2016 Mar 9;138(9):2941-4.
3. Jianing Cheng YL,WQ,MS,YL,WS,WDYZ. Mechanochemical synthesis and characterization of Mn-doped CsPbCl₃ perovskite nanocrystals. *Journal of Alloys and Compounds*. 2020; 822: 153615.
4. He W, Zhang Q, Qi Y, Moore J, Ray P, Pradhan N, Zhu X, Han F, Shahbazyan T, Dai Q. Synthesis and optical properties of doped CsPbCl₃ nanocrystals. *Journal of Nanoparticle Research*. 2021 Oct;23:1-1.
5. Yang D, Chu S, Wang Y, Siu CK, Pan S, Yu SF. Frequency upconverted amplified spontaneous emission and lasing from inorganic perovskite under simultaneous six-photon absorption. *Optics Letters*. 2018 May 1;43(9):2066-9.
6. Bhat AA, Khandy SA, Islam I, Tomar R. Optical, electrochemical and photocatalytic properties of cobalt doped CsPbCl₃ nanostructures: a one-pot synthesis approach. *Scientific Reports*. 2021 Aug 13;11(1):16473.
7. Yang D, Chu S, Wang Y, Siu CK, Pan S, Yu SF. Frequency upconverted amplified spontaneous emission and lasing from inorganic perovskite under simultaneous six-photon absorption. *Optics Letters*. 2018 May 1;43(9):2066-9.

8. Echeverría-Arrondo C, Alvarez AO, Masi S, Fabregat-Santiago F, Porta FA. Electronic, Structural, Optical, and Electrical Properties of CsPbX₃ Powders (X= Cl, Br, and I) Prepared Using a Surfactant-Free Hydrothermal Approach. *Nanomanufacturing*. 2023 May 19;3(2):217-27.
9. Fang S, Huang J, Li H, Nie J, Liu Z, Fang F, Zhong H. Sn²⁺ doping-induced large extra vibrational energy of an excited state for efficient blue emission in Cs₂SnCl₆:Bi. *Materials Advances*. 2023;4(10):2365-71.
10. Zhang H, Zhu L, Cheng J, Chen L, Liu C, Yuan S. Morphologically controlled synthesis of Cs₂SnCl₆ perovskite crystals and their photoluminescence activity. *Crystals*. 2019 May 18;9(5):258.
11. Yao Y, Zhang SW, Liu Z, Wang CY, Liu P, Ma L, Wei G, Kang F. Air stable and highly efficient Bi³⁺-doped Cs₂SnCl₆ for blue light-emitting diodes. *RSC advances*. 2021;11(42):26415-20.
12. Horiba Scientific. [Online]. [cited 2024. Available from: <https://www.horiba.com/gbr/scientific/products/detail/action/show/Product/labram-hr-evolution-1083/>.
13. Liao M, Shan B, Li M. In situ Raman spectroscopic studies of thermal stability of all-inorganic cesium lead halide (CsPbX₃, X= Cl, Br, I) perovskite nanocrystals. *The journal of physical chemistry letters*. 2019 Mar 1;10(6):1217-25.
14. Thesika K, Vadivel Murugan A. Microwave-enhanced chemistry at solid–liquid interfaces: synthesis of all-inorganic CsPbX₃ nanocrystals and unveiling the anion-induced evolution of structural and optical properties. *Inorganic chemistry*. 2020 Apr 14;59(9):6161-75.
15. Kaltzoglou A, Antoniadou M, Kontos AG, Stoumpos CC, Perganti D, Siranidi E, Raptis V, Trohidou K, Psycharis V, Kanatzidis MG, Falaras P. Optical-vibrational

- properties of the Cs₂SnX₆ (X= Cl, Br, I) defect perovskites and hole-transport efficiency in dye-sensitized solar cells. *The Journal of Physical Chemistry C*. 2016 Jun 9;120(22):11777-85.
16. Prasanna R, Gold-Parker A, Leijtens T, Conings B, Babayigit A, Boyen HG, Toney MF, McGehee MD. Band gap tuning via lattice contraction and octahedral tilting in perovskite materials for photovoltaics. *Journal of the American Chemical Society*. 2017 Aug 16;139(32):11117-24.
17. Chowdhury TH, Reo Y, Yusoff AR, Noh YY. Sn-Based Perovskite Halides for Electronic Devices. *Advanced Science*. 2022 Nov;9(33):2203749.

6. CONCLUSION

Ligand assisted reprecipitation (LARP) method has been successfully used to synthesize $\text{CsPb}_{1-x}\text{Sn}_x\text{Cl}_3$ ($x = 0, 0.25, 0.5, 0.75$) perovskite structures efficiently and at room temperature. The element Sn was successfully introduced into the host CsPbCl_3 using this method. This method requires precise control over temperature during the synthesis process. CsSnCl_3 could not be formed with this method indicating further research is required to identify the ligand, solvent or the temperature of synthesis. All the samples formed in cubic phase with $Pm\bar{3}m$ space-group except for Cs_2SnCl_6 which formed cubic phase with $Fm\bar{3}m$ space-group. All the sample except Cs_2SnCl_6 showed excellent cubic morphology while, Cs_2SnCl_6 showed octahedron morphology. The crystallite size was seen to vary between 32 nm to 41 nm for all $\text{CsPb}_{1-x}\text{Sn}_x\text{Cl}_3$ while the crystallite size for Cs_2SnCl_6 was seen to be 33 nm. All the sample showed absorption in the visible region of the light spectrum except for Cs_2SnCl_6 which has absorption in the UV range. The bandgap was found to vary from 2.89 eV to 2.76 eV for $\text{CsPb}_{1-x}\text{Sn}_x\text{Cl}_3$, while Cs_2SnCl_6 was found to have a bandgap of 3.2 eV. Photoluminescence spectra showed the emission peaks within the range of 400-500 nm indicating their use in making blue LEDs. Raman spectroscopy revealed three active modes for the samples for the $[\text{BX}_6]$ octahedra and the motion of the metal cation. In brief, this method can be used to synthesize halide perovskites in a efficient manner with a good morphology and satisfactory properties. In future, these samples can be used to try and synthesise single crystals for photovoltaic application.

